










The California-Kepler Survey. XI. A Survey of Chromospheric Activity through the Lens of Precise Stellar Properties

Howard Isaacson^{1,2} , Stephen R. Kane^{2,3} , Brad Carter² , Andrew W. Howard⁴ , Lauren Weiss⁵ , Erik A. Petigura⁶ , and Benjamin Fulton⁷ 

¹ 501 Campbell Hall, University of California at Berkeley, Berkeley, CA 94720, USA; hisaacson@berkeley.edu

² Centre for Astrophysics, University of Southern Queensland, Toowoomba, QLD, Australia

³ Department of Earth and Planetary Sciences, University of California, Riverside, CA 92521, USA

⁴ California Institute of Technology, Pasadena, CA 91125, USA

⁵ Department of Physics, University of Notre Dame, Notre Dame, IN 46556, USA

⁶ Department of Physics & Astronomy, University of California Los Angeles, Los Angeles, CA 90095, USA

⁷ NASA Exoplanet Science Institute/Caltech-IPAC, MC 314-6, 1200 E. California Boulevard, Pasadena, CA 91125, USA

Received 2023 July 26; revised 2023 October 13; accepted 2023 October 25; published 2024 January 16

Abstract

Surveys of exoplanet host stars are valuable tools for assessing population level trends in exoplanets, and their outputs can include stellar ages, activity, and rotation periods. We extracted chromospheric activity measurements from the California-Kepler Survey Gaia survey spectra in order to probe connections between stellar activity and fundamental stellar properties. Building on the California Kepler Survey's legacy of 1189 planet host star stellar properties including temperature, surface gravity metallicity, and isochronal age, we add measurements of the Ca II H and K lines as a proxy for chromospheric activity for 879 planet hosting stars. We used these chromospheric activity measurements to derive stellar rotation periods. We find a discrepancy between photometrically derived and activity-derived rotation periods for stars on the Rossby Ridge. These results support the theory of weakened magnetic braking. We find no evidence for metallicity-dependent activity relations, within the metallicity range of -0.2 to $+0.3$ dex. With our single epoch spectra we identify stars that are potentially in Maunder minimum-like state using a combination of $\log(R'_{HK})$ and position below the main sequence. We do not yet have the multiyear time series needed to verify stars in Maunder minimum-like states. These results can help inform future theoretical studies that explore the relationship between stellar activity, stellar rotation, and magnetic dynamos.

Unified Astronomy Thesaurus concepts: [Stellar activity \(1580\)](#); [Exoplanet astronomy \(486\)](#); [Stellar chromospheres \(230\)](#)

Supporting material: machine-readable table

1. Introduction

The study of stellar chromospheres was championed in the late 1960s by the Mt. Wilson S -value project (Vaughan et al. 1978; Duncan et al. 1991). With a dedicated telescope for daily observations, the Mt. Wilson team began a series of observations that would last decades culminating in the study of stellar activity cycles and comparison to the solar activity cycle. The legacy of the Mt. Wilson HK project was expanded from the photomultiplier era to the era of charge coupled devices by additional studies of stellar activity cycles including those conducted by Henry et al. (1996; 815 stars), Wright et al. (2004; 1200 stars), Hall et al. (2007; 143 stars), Isaacson & Fischer (2010; 2630 stars), and more recently Gomes da Silva et al. (2021; 1674 stars). These surveys were often secondary to the primary science objectives (Hall et al. 2007; excepted) of searching for exoplanets and measuring their masses via high-resolution spectroscopy and precise radial velocities (RVs). For example, the importance of understanding stellar activity as a possible false-positive scenario for RV planet mass detection was a primary concern since the first exoplanet discovery (Mayor & Queloz 1995). In addition to the search for direct correlations between RVs and stellar activity cycles over the

timescale of decades (Wright et al. 2008; Fulton et al. 2015), sophisticated analyses such as the FF' method, Gaussian processes, and other signal processing algorithms can be employed on data spanning shorter timescales to disentangle the complex relationships that planets have on stars gravitationally from stellar activity due to surface inhomogeneities (Aigrain et al. 2012; Howard et al. 2013; Pepe et al. 2013). However, sophisticated signal processing techniques can sometimes overfit the data, and their results should be interpreted with caution (Blunt et al. 2023). When additional information beyond stellar spectra are available, such as space-based photometry from Kepler, K2, or the Transiting Exoplanet Survey Satellite (TESS; Kosiarek & Crossfield 2020), ever smaller planets can be characterized with RVs from instruments such as the High Resolution Echelle Spectrometer (HIRES; Akana Murphy et al. 2021) or refuted with instruments such as Habitable Planet Finder (Lubin et al. 2021). Analysis of stellar flares in photometric data, along with activity metrics from spectra such as $H\alpha$ can be used to study planetary habitability. Su et al. (2022) used $H\alpha$ measurements from LAMOST's low-resolution (1026 stars) and medium-resolution spectra (158 stars) plus light curves from Kepler, K2, and TESS host stars, and assessed both atmospheric burn off and recovery.

The impact of stellar activity observations has led to a greater understanding the relationship of stellar activity, rotation periods, and age. Noyes et al. (1984) laid the foundation for studying connection between activity,



Original content from this work may be used under the terms of the [Creative Commons Attribution 4.0 licence](#). Any further distribution of this work must maintain attribution to the author(s) and the title of the work, journal citation and DOI.

convection and rotation, showing that rotation periods correspond to certain levels of activity and both are related to the convective action in solar-type main-sequence stars. Remarkably, the study used only 40 stars, with what would now be considered primitive determinations for stellar temperature and mass that were based on $B - V$ colors, without parallaxes or high-resolution spectra. Identification of the Rossby number, the ratio of the stellar rotation period to the convective turnover time, was a critical piece of the rotation-activity-age puzzle. This early work, focusing primarily on solar-like, main-sequence stars, was summarized by Duncan et al. (1991) who provided the activity catalog for a large number of stars, and Baliunas et al. (1995) who focused on 111 Sun-like stars. To extend the age-activity relations beyond solar-type stars, Mamajek & Hillenbrand (2008) determined ages by analyzing young star clusters with ages between 200 Myr and 7 Gyr open clusters using both X-rays and chromospheric activity measurements. As stars age, the stellar wind, and more generally magnetic activity, transports angular momentum away from the star, resulting in decreasing rotation periods and lower activity levels. By adding star clusters with various well-known ages, Mamajek & Hillenbrand (2008) quantified the relationship between stellar spindown and stellar age for stars much younger than the Sun. With the use of Gaia proper motion, new young clusters have been identified, adding to the collection of age and activity analyses. Curtis et al. (2020) used open clusters with ages between 0.7 and 1.4 Gyr to identify a pause in the spindown relationships that is especially prominent for lower-mass stars. The change in spindown can be accounted for tuning core-envelope models, but other explanations remain possible.

The Kepler era of space-based photometric surveys led to the detection of over 4000 transiting planet candidates (Borucki et al. 2011a, 2011b; Batalha et al. 2013; Thompson et al. 2018). While the first exoplanet systems detected by Kepler were confirmed by ground-based follow-up observations (Borucki et al. 2010; Batalha et al. 2011), it was the large-scale survey of $\sim 200,000$ stars by Kepler that led to the most important results.

The California-Kepler Survey (CKS), a magnitude-limited spectroscopic survey of 1189 Kepler host stars was undertaken with the focus on improving the uncertainty in stellar radius, and the associated planetary radii. Analysis of high-resolution stellar spectroscopy using local thermodynamic equilibrium (Valenti & Fischer 2005) is capable of determining fundamental stellar properties and can be combined with stellar evolution models to determine stellar mass and radius to a typical precision of 10% and as low as 2% (Johnson et al. 2017; Berger et al. 2020b). The uniform, and homogeneous data set of high-resolution spectra from the Keck I telescope and HIRES instrument (Petigura et al. 2017) has allowed for detection of the detailed structure in the radius distribution for planet sizes between 1 and 4 R_{Earth} (Fulton et al. 2017). The CKS data set has allowed for a series of papers including beyond the planet radius gap including detailed analysis of systems with multiple transiting planets Weiss et al. (2018), refinement on the minimum mass extra-solar nebular (Dai et al. 2020), and analysis showing that the Kepler field has similar metallicity to the solar neighborhood (Petigura et al. 2018).

The eventual addition of Gaia parallaxes further refined the stellar properties of the full Kepler sample, their planets' radii, and more broadly planet occurrence (Fulton & Petigura 2018; Hsu et al. 2019). With precise Gaia distances, the dominant

source of error on the planet radius, now on average 5%, becomes the photometry (Petigura 2020), a major transition compared to the first transiting planets measured with Kepler data. Theoretical studies have suggested that the substructure in the planet radius distribution is due to photoevaporation that occurs in the first 100 Myr of planet formation (Lopez & Fortney 2013; Owen & Wu 2013; Chen & Rogers 2016). Observational studies calculating precise ages reveal that planet radius changes may continue beyond 1 Gyr when considering the entire Kepler planet sample (Berger et al. 2020a) and well-defined subsamples (David et al. 2022). The radius gap is also reported observationally by Van Eylen et al. (2018) in an analysis of planet hosts studied with asteroseismology.

The paper is laid out as follows. Section 2.1 describes how we derived S values from the HIRES spectra, and Section 2.2 describes our star and planet sample. Section 3.1 shows how the planet properties of CKS-Gaia relate to new stellar activity metrics. Section 3.2 explores how the rotation periods determined from Kepler photometry relate to activity metrics from this sample. Activity measurements are correlated with fundamental stellar properties in Section 3.3. In Section 3.4 we discuss ages derived from $\log(R'_{\text{HK}})$ values and we touch on the least active stars in our sample and discuss implications in Section 3.5. Finally, Section 3.6 explores activity and our Kepler planet sample.

2. Methods

2.1. S -value Extraction and Calibration

We follow the method of Isaacson & Fischer (2010) to extract the flux values in the cores of the Ca II H and K lines and continuum regions redward and blueward of the H and K absorption features (Equation (1); Vaughan et al. 1978). While this extraction method has been used to analyze post-upgrade HIRES data dating back to 2005, we modified the existing algorithm to optimize the signal-to-noise ratio (S/N) of single-epoch spectra that range from 6 to 10 per reduced pixel. Isaacson & Fischer (2010) used an S/N cutoff of 5, but only 2% of spectra were below S/N of 10, so the extraction routine was not well tested for S/N = 5–10. Examples of the Ca II H and K line cores for stars with the highest, median, and lowest S -values in our sample are shown in Figure 1. This is distinct from the most and least active stars, which are measured by $\log(R'_{\text{HK}})$. Note that low S/N makes the extraction of the fluxes more challenging in spectra with S/Ns of 5–10 in the continuum sections. In this work, we spline the National Solar Observatory (NSO) solar atlas onto the HIRES rest-frame wavelength solution, and use it as the template to align all other spectra. The Isaacson & Fischer (2010) spectral extraction method was optimized for measuring differential S -values of the same star using a high-S/N template, the current analysis utilizes the NSO template for all stars in this sample to ensure the absolute scale is as accurate as possible for the single epochs of the CKS-Gaia sample.

$$S_{\text{HK}} = \frac{H + K}{R + V} \quad (1)$$

S -values are calculated by summing the flux in the cores of the Ca II H and K lines and dividing by the flux in two continuum sections redward and blueward of the line cores (Figure 2). The value of an isolated S -value is difficult to interpret across different spectral types because the intensity of the neighboring regions varies with stellar type, which means

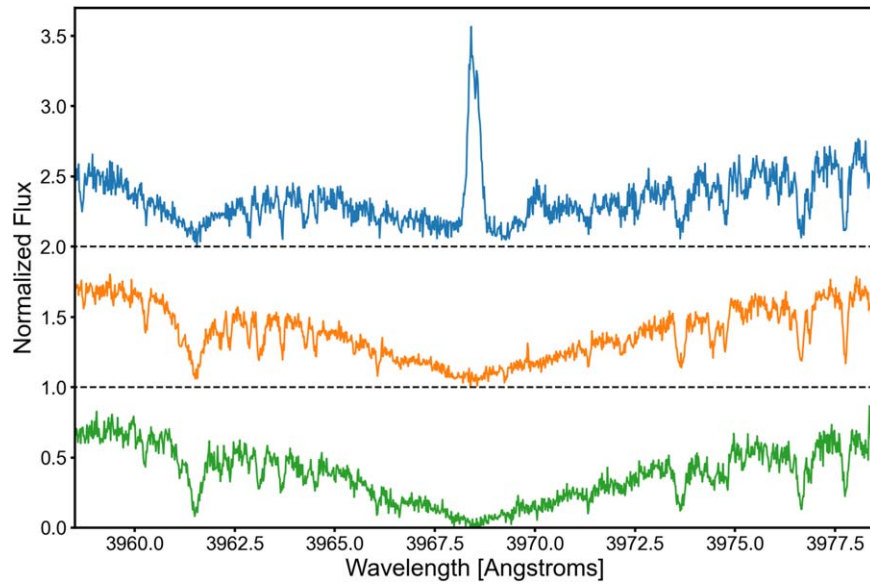


Figure 1. The Ca II H-line is shown for the stars with the highest, median, and lowest S -values from top to bottom. They are KOIs-3497, 700, and 629. The S/N s of 5–10 per pixel in the continuum sections for these stellar spectra makes the spectral extraction challenging. For active stars, the reversal in the core of the Ca H-line is obvious and rises above the continuum. Small changes in the activity level of low-activity stars are challenging to detect due to the lower flux in the line cores.

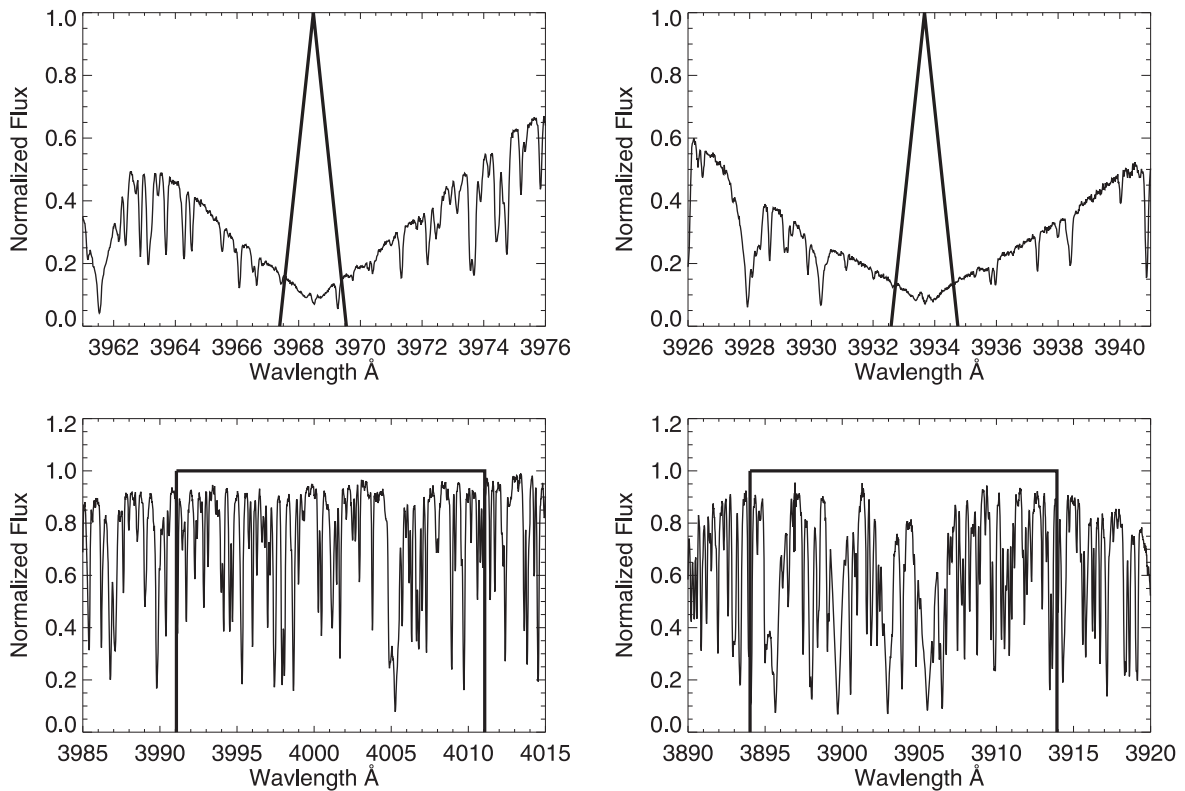


Figure 2. Clockwise from top left: the Ca II H and K lines, and the two continuum sections on either side of the H and K lines, dubbed V (centered at 4000 Å) and R (centered at 3905 Å) sections. The two 20 Å continuum sections are used to calibrate the variable flux in the 1 Å weighted sections in the line cores. Extracting the spectral segments in this way allows for calibration to the Mt. Wilson scale and comparison to other activity surveys.

the raw S -value index is sensitive to both chromospheric emission and overall SED. So we calculate $\log(R'_{HK})$, a metric of chromospheric activity that is comparable across stars with different T_{eff} . $\log(R'_{HK})$ is defined as the base-10 logarithm of the chromospheric portion of the flux in the Ca II H and K line cores relative to the bolometric flux of the star (Noyes et al. 1984). We use the Ca II H and K line flux to measure the

nonthermal heating that is related to magnetic activity in the star. By accurately accounting for and subtracting the photospheric contribution to the flux in the cores of the Ca II H and K line cores, we can compare activity across a range of effective temperatures.

With this new flux normalization and extraction method, we require a new calibration to the Mt. Wilson Scale to ensure we

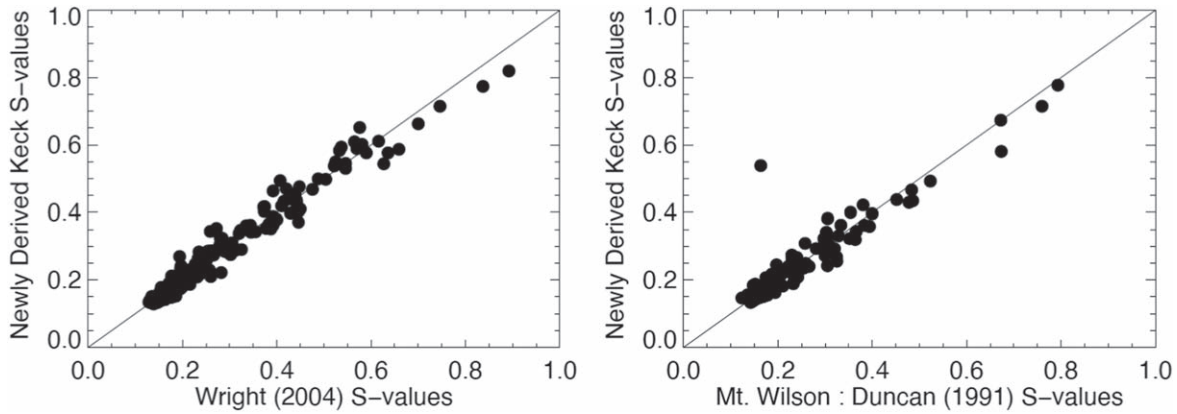


Figure 3. By selecting stars that have been observed with HIRES by CPS and by the Mt. Wilson survey, we can determine the coefficients needed to convert flux values to S -values. (Left) We assess our S -values for consistency by comparing our newly created values with those published in Wright et al. (2004), whose values were calculated from spectra collected on the previous HIRES detector, pre-2005. The S -values on the y -axis were created with the coefficients determined by fitting our newly extracted flux values to the Wright S -values. Four-hundred and forty-seven stars were used in this comparison. The standard deviation of the residuals is 0.020. (Right) The Mt. Wilson values from Duncan et al. (1991) are plotted against our newly determined values for 154 overlapping stars. Scatter in the relation is due to observing stars at different points in their activity cycles as well as imperfect accounting of the blaze function. The star at [0.2, 0.6] is a known outlier, HD 137778, detailed in Wright et al. (2004). If we include HD 137778, the standard deviation of the residuals is 0.044. Removing the single outlier reduces the standard deviation to 0.024.

can compare our activity metrics on a standard scale. Using a procedure similar to Isaacson & Fischer (2010), we use four coefficients and perform a least-squares fit for two free parameters, C_1 and C_4 in Equation (2), with two of the coefficients, C_2 and C_3 determined by the ratios of the H to K line fluxes and R to V line fluxes. The final coefficients are shown in Equation (2) and were found using 154 stars that were observed on HIRES and Mt. Wilson. We restrict the calibration stars to T_{eff} between 4700 and 6500 K with $V \sin(i) < 10 \text{ km s}^{-1}$ and a $\log(g)$ greater than 4.0, matching the demographics of the majority of the CKS-Gaia sample.

$$S_{\text{HK}} = C_1^* \frac{(H + C_2^*K)}{(R + C_3^*V)} + C_4 \quad (2)$$

$$S_{\text{HK}} = 22.5^* \frac{(H + 1.01019^*K)}{(R + 1.26134^*V)} - 0.006 \quad (3)$$

The newly created HIRES S -values are plotted against the Duncan et al. (1991) S -values, showing a standard deviation of the residuals of 0.023 (Figure 3, right panel). This is comparable to the Isaacson & Fischer (2010) S -values, that showed a scatter of 11% when calibrated to the Mt. Wilson values. We attribute the larger scatter in the 2010 work to the broader range of stars in that sample, both in terms of activity and T_{eff} , compared to this work. We verify our calibration by comparing our new S -values of 447 non-Kepler stars that also have S -values in the Wright et al. (2004) sample of planet search stars observed on HIRES prior from 1995–2004. The standard deviation of the residuals is 0.020 (Figure 3, left panel). We adopt 0.02 as the calibration uncertainty, similar to survey calibration uncertainty found by Mittag et al. (2013).

We verified continuity in the activity scale from the Isaacson & Fischer (2010) method to the new NSO method described in the paper by plotting both sets of S -values for two stellar activity standards, Tau Ceti and HD 60532 (Figure 4). Gomes da Silva et al. (2021) noted that the chromospheric standard star Tau Ceti varies by 0.83% or a dispersion of 0.0015, and recommended using HD 60532 as well, with a scatter of only 0.36%, and absolute dispersion of 0.0005. This tiny variation

over time makes HD 60532 an excellent standard star for checking single instrument Ca II H and KS-value precision.

There is a small offset between the values from the Isaacson & Fischer (2010) method and our new HIRES-NSO method that is visible for both standard stars. With the HIRES-NSO method, Tau Ceti shows a median S -value of 0.1720 with a standard deviation of 0.0023. The HIRES-NSO derived S -values for HD 60532 show a median value 0.1197 with a dispersion of 0.0031. For Tau Ceti, the Isaacson & Fischer (2010) method yields a median of 0.1670, with a standard deviation of 0.0016. For HD 60532 the median is 0.1231 with a standard deviation of 0.0029. The new S -values for Tau Ceti and HD 60532 are offset by +0.005 and -0.004 , respectively. The offsets are due to scatter in the calibration and the amplitude of the offset is similar to the amplitude of the scatter. Our uncertainties are consistent with previous works. For example, Tau Ceti shows very little long-term variation but calibration uncertainties result in published values of 0.168 from Wright et al. (2004) and 0.175 from Duncan et al. (1991). The performance of these standard stars gives us confidence in our extraction method and quantifies the error in our calibration.

Our distribution of S -values extends to lower values than previous surveys, with a tale toward very low activity that reaches $\log(R'_{\text{HK}}) = -6.0$ (Figure 5). We choose a value of $\log(R'_{\text{HK}}) = -5.50$ as the lowest value that should be considered reliable. In Section 3.5 we discuss very inactive stars, and WASP-12 is an example of a star with the exceptionally low value of $\log(R'_{\text{HK}})$ of -5.50 . The low value is thought to be due to absorption beyond the chromosphere of the star (Fossati et al. 2013). Stars in our sample with $\log(R'_{\text{HK}})$ values below -5.50 should be considered very inactive, but these values likely underestimate their activity.

For the CKS-HK sample, most stars have a single observation, limiting our knowledge of the long-term behavior of these stars. For stars with two observations, we choose the one with higher S/N. For stars observed more than twice, such as those with multiple epochs for RV follow-up, we choose the median S -value. Time-series S -values for these stars are available in Weiss et al. (submitted). The coolest stars in our

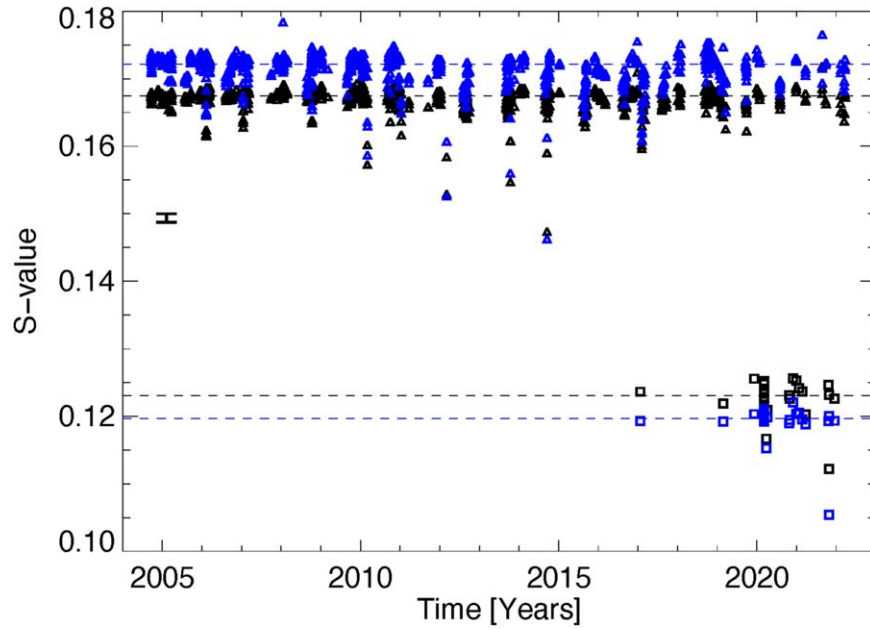


Figure 4. For the standard stars Tau Ceti (top set, triangles) and HD 60532 (bottom set, squares), S -values are calculated using the Isaacson & Fischer (2010) routine (black) and from the new HIRES-NSO routine (blue). The average values of 0.1670 ($\log(R'_{\text{HK}}) = -4.980$) and 0.172 ($\log(R'_{\text{HK}}) = -4.954$), respectively, are plotted as dashed lines. The offset of 0.005 or 3% is due to different methods for addressing the blaze function as well as calibration errors. (The Mt. Wilson average value for Mt. Wilson is 0.175, compared to our HIRES-NSO median value of 0.172.) The standard deviations of the Isaacson & Fischer (2010) values and the newly derived values for Tau Ceti are 0.0016 and 0.0024. For HD 60532, they are 0.0029 and 0.0031. The single-epoch uncertainty of 0.03 is depicted at [2005, 0.015]. We use 942 observations of Tau Ceti. A representative error bar 1% as determined by the scatter of Tau Ceti and HD 60532, two S -value standards, is shown at [2005, 0.15].

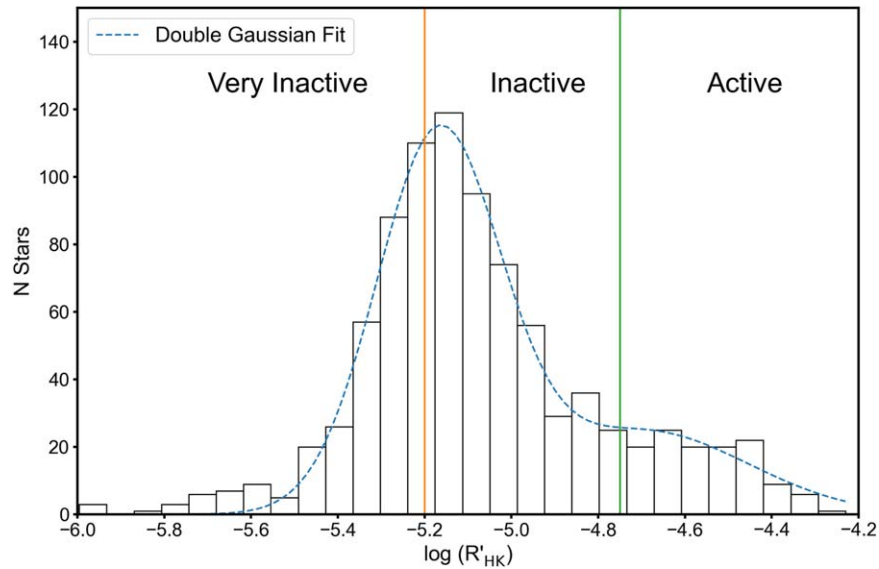


Figure 5. Double-Gaussian fit for the full CKS stellar sample of 893 stars.

sample have spectra that differ most significantly from the Sun, and we find that the S -values for these stars still meet our quality standards. Another limitation of using a single epoch in time to measure stellar activity is that we measure the activity at an unknown phase of the rotation period and activity cycle. This challenges our search for stars that are exceptionally inactive, in Maunder minimum or magnetic minima states (Section 3.5). We rely on the statistical power, rather than time series, of our sample for the analysis of fundamental stellar properties, activity, and rotation periods. Without time-series spectra to monitor long-term activity cycles, we are unable to make comparisons of years long cycles with rotation periods such as Brandenburg et al. (2017) and Metcalfe et al. (2016).

Instead, our analysis is similar to Zhang et al. (2020), which also utilizes single-epoch spectroscopy to assess activity for 59,816 stars. Our smaller sample has a T_{eff} uncertainty of 60 versus 100 K for the Large Sky Area Multi-Object Fiber Spectroscopic Telescope (LAMOST) sample (Petigura et al. 2017), and we focus our attention on the rotation periods from David et al. (2021).

2.2. The CKS-HK Sample

The CKS sample has several components including a magnitude-limited sample, with a cutoff at a Kepler magnitude of 14.2, and a collection of fainter stellar host stars that includes

habitable zone planets (Borucki et al. 2013), multiplanet systems (Lissauer et al. 2014; Rowe et al. 2014), and ultra-short-period planets (Sanchis-Ojeda et al. 2014). The habitable zone planets and the multis fainter than 14.2 tend to have lower S/Ns and are often omitted from our sample for having insufficient data quality in the bluer wavelengths where the Ca II H and K lines reside. To define the CKS-Gaia sample, Fulton & Petigura (2018) make a similar magnitude restriction because the primary sample selection for stars fainter than $V \sim 14.2$ was nonuniform. We choose to begin with the sample of 1189 planet stars hosting 1896 total planets from Fulton & Petigura (2018) and make additional quality cuts for our analysis. We did not include the stars from the recent CKS-Cool project (Petigura et al. 2022) because the target S/N is too low at 4000 Å to precisely measure the Ca II H and K line fluxes.

In order to ensure sufficient quality of the S -value activity metric, we made restrictions on the S/N near the Ca II H and K lines and on the local seeing conditions for each observation. The CKS-Gaia S/N for HIRES spectra was chosen to be ~ 40 per pixel at 5000 Å. This choice impacts the S -values resulting for cooler stars that have lower S/N in the Ca II H and K region compared to hotter stars due to inherent differences in their blackbody spectra. Beginning with the CKS-Gaia results (Table 1 from Fulton & Petigura 2018), which has 1189 planet host stars, we remove 180 observations that have $S/N < 5 \text{ pixel}^{-1}$ in the continuum regions near the Ca II H and K lines. In most cases, we use the same spectra as the CKS-Gaia project; however, there were 25 stars with higher-S/N spectra, collected more recently, that were available. From the 2D echellogram, we measured the seeing value for each observation and removed observations with seeing greater than $1''.6$, ensuring high-quality measurements (Baum et al. 2022). The HIRES spectrometer, a slit-fed spectrograph that uses an echelle grating as the cross-dispersing optic, results in a 2D echelle format in which the orders become closer together toward bluer wavelengths. (Spectrographs with cross-dispersing prisms have orders that are closer together in the red). Since we use the C2 decker ($0''.87 \times 14''.0$) for observations of faint stars in order to remove background sky flux (Batalha et al. 2011), when a faint star ($V > 11$) is observed in poor seeing conditions, the bluest orders overlap, causing cross order contamination and a poor-quality S -value measurement. Removing 109 observations with poor seeing values and three stars that have no stellar mass or radius leaves 900 planet host stars with well-characterized stellar properties and S -values. Three stars have no $\log(g)$ value. Fourteen stars have an S -value lower than 0.10, chosen as a minimum value for calculating $\log(R'_{\text{HK}})$, leaving 879 host stars. We define this as our CKS-HK stellar sample.

Binary star systems can challenge studies of stellar activity due to tidal interaction or spectral contamination, or with spectral contamination. To mitigate binary star contamination, stars with a detected secondary spectrum, with flux ratios as low as 1% of the primary, using the technique of Kolbl et al. (2015) were identified by Fulton et al. (2015) as planet false positives and are excluded as such.

The CKS-HK catalog of chromospheric activity is quite different compared to RV surveys of planet search stars. While most RV surveys focus on either M-dwarfs or FGK stars providing large catalogs of high-resolution spectra, the stars in these surveys typically have an unknown number of short-

period planets with planet radii from 1–4 Earth-radii (Rosenthal et al. 2021). In comparison, every star in our sample has one or more known transiting planets, and the distance to the average Kepler field star is about a kiloparsec rather than a 1–200 pc for typical RV survey stars.

2.2.1. The CKS-HK Planet Sample

In addition to the quality metrics applied to the CKS-HK stellar sample, for analysis involving planet properties, we make further qualifications. The CKS-HK planet sample will be defined by the quality cuts that are described in Section 2.1 and further quality cuts that depend on the planet properties in these systems. Much of the analysis focuses on planets smaller than $4.0 R_{\text{Earth}}$. We define this as our CKS-HK planet sample.

2.3. Literature Data

2.3.1. Kepler Stellar Rotation Curves

The field of stellar rotation period analysis has richly benefited from the Kepler 30 minute cadence with near continuous data collection for 90 days of a typical Kepler quarter, up to 4 yr over the life of the mission. While ground-based photometric surveys had been critical in building our understanding of stellar rotation periods (Duncan et al. 1991; Henry et al. 1996), Kepler has grown the number of available stellar rotation periods into the tens of thousands (McQuillan et al. 2014).

Novel techniques applied to light curves can quickly analyze vast amounts of photometry. The auto-correlation function (ACF; McQuillan et al. 2014) was used to create a catalog of rotation periods for 30,000 stars ranging from 0.2–70 days across stellar masses from 0.1–1.3 M_{\odot} . Angus et al. (2018) used a machine-learning technique, trained on that catalog, to determine rotation periods for Kepler objects of interest (KOIs), which we use in Section 3.2. Santos et al. (2021) used a combination of wavelet analysis, ACFs, and machine learning to further study the rotation periods of Kepler stars.

Recently, David et al. (2022) examined Kepler rotation periods from Walkowicz & Basri (2013), McQuillan et al. (2014), Mazeh et al. (2015), and Angus et al. (2018) resulting in the identification of the “Rossby Ridge,” a relationship between the T_{eff} and stellar rotation period. The Rossby Ridge results support the stellar spindown theory of weakened magnetic braking (WMB) as formulated in van Saders et al. (2016), which is a deviation from the spindown relationships that govern young stars until the ages of a few gigayears. We build upon vetted rotations periods of the CKS-Gaia sample from David et al. (2021), adding the chromospheric activity measurements from the Ca II H and K lines to explore $\log(R'_{\text{HK}})$ and its relation to stellar rotation periods and stellar spin down in the Rossby Ridge in Section 3.2.

2.3.2. The CKS-HK Stellar Rotation Sample

The CKS-HK rotation sample begins with the CKS-HK stellar sample, and is refined based on the quality of the determination of the photometric rotation periods from Kepler. We use this sample to examine activity-rotation relations and stellar effective temperature, metallicity, and stellar surface gravity. The stellar rotation analysis will require dividing the sample by stellar type, evolution, and [Fe/H]. In order to utilize the most well-determined stellar rotation periods, we keep only

the reliable stellar rotation periods from Kepler photometry compiled and vetted by David et al. (2021) to define the CKS-Gaia sample of rotation periods. The quality of rotation periods are labeled 0, 1, 2, and 3 as having no periodicity, an ambiguous period, a reliable period and a highly reliable period, respectively. We take the CKS-HK stellar sample of 879 stars, with valid chromospheric activity measurements and the vetted rotation periods, to finalize our CKS-HK rotation period sample with 168, 325, 216, and 184 stars and reliability ranks of 0, 1, 2, and 3, respectively.

3. Results and Discussion

We begin our analysis by examining the relationships between our new $\log(R'_{\text{HK}})$ measurements of the chromospheric activity and the fundamental stellar properties from CKS-Gaia.

3.1. T_{eff} , $\log(g)$, $[\text{Fe}/\text{H}]$, and $\log(R'_{\text{HK}})$

We examine the full distribution of $\log(R'_{\text{HK}})$ for our stellar sample, and model it with a two-Gaussian fit (Figure 5). As a function of the stellar properties T_{eff} , $[\text{Fe}/\text{H}]$, and R_* in Figure 6. To allow for quantitative comparisons between surveys (such as Santos et al. 2021), we model three subsets of our sample as both single- and double-Gaussian distributions. The top panel of Figure 6 shows the distribution of $\log(R'_{\text{HK}})$ divided at T_{eff} values of 6000 and 5400 K, with the hotter F-stars on the left and cooler K-dwarfs on the right. In the middle panel, we divide stars into bins of metallicity at +0.1 and -0.1 dex, with the most metal-rich stars of the left and solar metallicity stars in the middle. The $\log(R'_{\text{HK}})$ distribution as a function of stellar radii is divided at 0.9 and 1.1 R_{\odot} with solar radius-like stars in the bottom-middle panel. Gaussian fitting results for the full sample, and the subdivided sample are compiled in Table 1.

Sun-like stars are a common focus in activity analyses, and our study focuses on stars between 4800 and 6250 K. Stars with temperatures above the Kraft Break at T_{eff} of 6250 K have thinning convective zones, dividing fully radiative and partially convective stars (Kraft 1967). Fully radiative stars are magnetically different than those below the Kraft Break because they lack a tachocline that is thought to be the critical to the production of magnetic activity. The study of rotation and convection near the Kraft Break is an active field of study (Metcalf & Egeland 2019) and is relevant in our rotation period analysis. The histogram of $\log(R'_{\text{HK}})$ colored via stellar radius (Figures 5, bottom right) complements the $\log(g)$ histogram (upper right) showing a more intuitive value than stellar surface gravity. Generally, the stars with the largest radii in our sample are evolved and are also the least active. We will discuss the relationship between $[\text{Fe}/\text{H}]$ and stellar rotation periods in Section 3.3.2.

We examine the CKS-HK stellar sample broadly in Figure 7 by plotting the CKS-HK stellar properties sample as a function $\log(R'_{\text{HK}})$. In the temperature plot, we see the most active stars are cooler than the Sun, and all of the inactive stars have super-solar temperature. The relationships between stellar surface gravity and stellar radius relations to $\log(R'_{\text{HK}})$ reveal the most active stars in our sample are on the main sequence and near to 1.0 R_* , consistent with Figure 8. Viewing the sample in T_{eff} versus $\log(g)$ space, the subgiant population rises above the main sequence as $\log(g)$ decreases (Figure 8). While the division between subgiant and main-sequence stars is ill-defined, we will use various cutoffs for $\log(g)$ in the next few

Sections, including $\log(g) = 4.0$. The color scaling shows that most stars are in the “inactive” or “very inactive” categories. The most active stars exist along the lower envelope, with the highest $\log(g)$ values, as expected for stars that lie nearest to the zero-age main sequence. For the rotation period analysis in Section 3.2 and the study of the least active stars (Section 3.5), we will focus on main-sequence stars rather than subgiants.

When testing for a correlation between chromospheric activity and metallicity, we might expect to see metal-rich stars, which tend to be younger than metal-poor stars, and are also more active. This property is visible in the bottom-left panel of Figure 7, which shows a fairly smooth distribution around the average $\log(R'_{\text{HK}})$ and $[\text{Fe}/\text{H}]$, with a slight overabundance of active stars that are metal-rich.

The least active stars are examined in detail in Section 3.5, and we search for candidates for stars that are in Maunder minimum or magnetic minimum (MM) type states (Eddy 1976; Saar 2011). Metallicity is also thought to be a factor in the study of stellar rotation periods, as the metal content of the star can affect the depth of the convective zone, and therefore the convective turnover time and rotation period (see Section 3.3.2).

3.2. Activity and Stellar Rotation Period

Decades-long observations of chromospheric activity measurements have identified relationships between chromospheric activity and stellar rotation, especially for solar-like stars. Noyes et al. (1984) formalized conclusions into equations that can be used to predict the rotation period based upon the average chromospheric activity of a star. By focusing on main-sequence Sun-like stars, the Mt. Wilson studies were able to isolate variables such as stellar $\log(g)$, T_{eff} (using $B - V$ as a proxy), and to an unknown extent, $[\text{Fe}/\text{H}]$. Wright (2004) speculated that spectral synthesis and precise stellar abundances (Valenti & Fischer 2005) would assist in finding very inactive stars. Stellar activity in the least active stars revealed that changes in $\log(g)$ due to stellar evolution is an important variable when identifying very inactive stars. Saar (2011) showed that stellar metallicity has an impact on both the minimum activity of a star and on the stellar rotation period. Additional metal content in a star changes the opacity and is perhaps more important when the convective zone is thin, such as in stars near the Kraft Break. Amard & Matt (2020) used theoretical models with stellar masses of 0.8, 1.0, and 1.3 M_{\odot} and $[\text{Fe}/\text{H}]$ between -0.5, and +0.5 and show that, metallicity is indeed an important variable to consider when calculating rotation period. They confirm that the impact is more significant near the Kraft Break, where small changes in metallicity affect the convective turnover time and have a larger impact due to the thinner convective zone.

In an observational test of those theoretical models, Avallone et al. (2022) used Kepler rotation periods, APOGEE data, and Gaia parallaxes to analyze rotation periods for stars mostly hotter than 6250 K, the Kraft Break. They found no rotation dependence on metallicity but noted the difference in T_{eff} for the two samples. The CKS-HK sample is well populated between 0.7 and 1.3 M_{\odot} , and we analyze the metallicity in the range 0 + 0.2 to -0.2 as well as, T_{eff} , R_* , and Kepler rotation periods in Section 3.3.2. The metallicity dependence is explored along with other fundamental stellar parameters, and we consider the activity derived rotation periods in the same context.

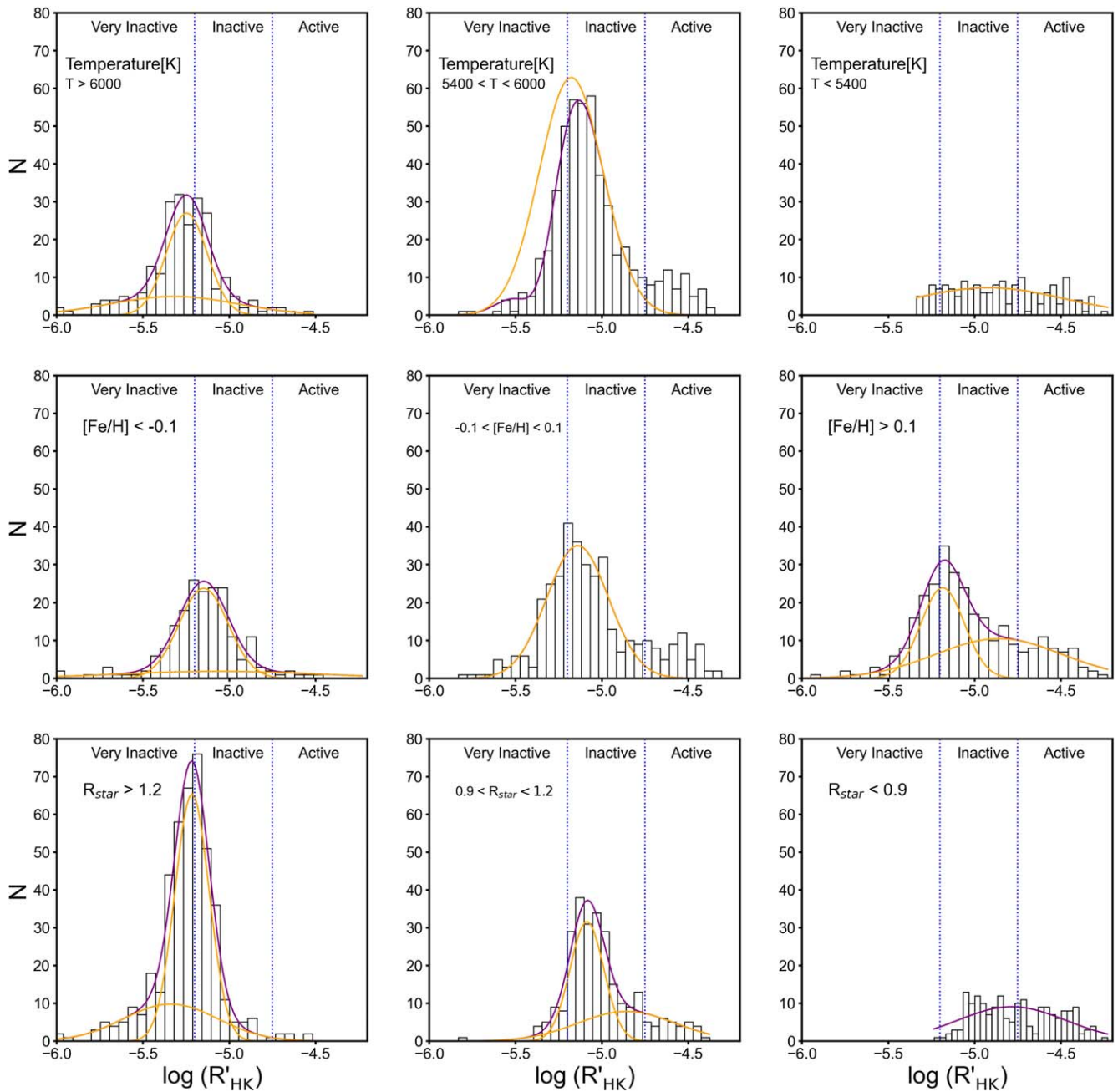


Figure 6. For each stellar property and property bin, the data are shown in the histogram, and the two-model Gaussian fit is shown in purple, with component Gaussians in yellow. A single-component Gaussian fit was preferred for the coolest bin of T_{eff} , the middle bin of $[\text{Fe}/\text{H}]$, and the bin of smallest R_* . Top row: T_{eff} separates the three panels from left to right with break points at 6000 and 5400 K. Middle row: $[\text{Fe}/\text{H}]$ separated from highest to lowest with break points at -0.1 and $+0.1$. Bottom row: R_* is plotted from the largest bin to the smallest with break points at 0.9 and $1.2 R_{\odot}$. The values of the fitted Gaussians are shown in Table 1.

3.2.1. Rotation Periods for the CKS-HK Sample

Beginning with the CKS-HK rotation sample defined in Section 2.3.2, we compare how the Noyes et al. (1984) rotation-activity relations used to calculate a stellar rotation period from $\log(R'_{\text{HK}})$ to stellar rotation periods recovered from Kepler photometry (David et al. 2021). We explore both methods of determining rotation periods and how they relate to the precise stellar properties from CKS-Gaia. Compared to the CKS techniques used to determine stellar properties to those used in Noyes et al. (1984), we have much more powerful tools in the form of high-resolution spectroscopy, to determine stellar

surface gravity and metallicity. We also have a broader range of stellar temperatures, which will expose the bias of solar-like stars when using the rotation periods derived from activity.

To visually confirm the relationship between activity and rotation, we plot $\log(R'_{\text{HK}})$ versus the Kepler rotation period in Figure 9. As a function of $\log(R'_{\text{HK}})$, we plot 215 stars with grade 2, “reliable,” stellar rotation periods from David et al. (2021) in the left panel and 185, grade 3, “highly reliable” rotation periods in the right panel. The color scale shows stellar effective temperature from 4800–6400 K, the full range of the CKS-HK sample. If a strong correlation between rotation

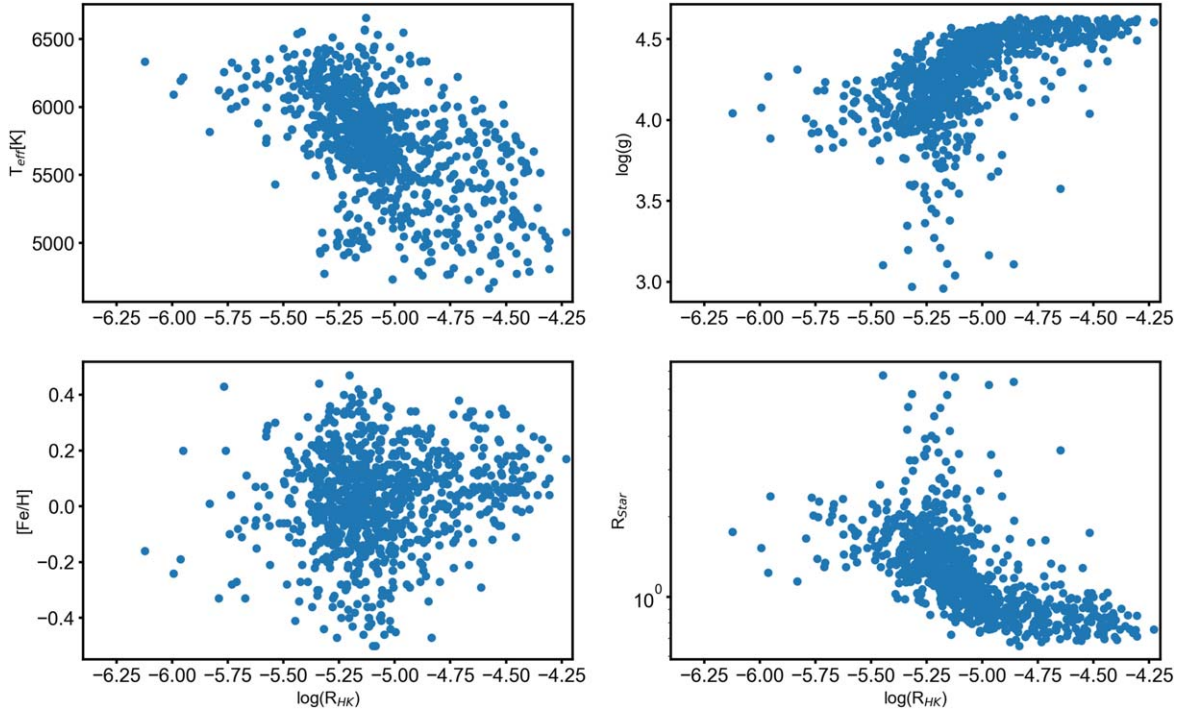


Figure 7. $\log(R'_{\text{HK}})$ is plotted on the x -axis for all plots (more active stars are to the right), and fundamental stellar parameters are plotted on the y -axis. Top left: $\log(R'_{\text{HK}})$ vs. T_{eff} shows that more active stars tend to be cooler. Top right: $\log(R'_{\text{HK}})$ vs. $\log(g)$ reveals that subgiants are sparse and are inactive ($\log(R'_{\text{HK}}) < -5.1$), which are lower on the plot. Most main-sequence stars have a range of activities. Bottom left: $\log(R'_{\text{HK}})$ vs. $[\text{Fe}/\text{H}]$ shows a balanced distribution with more active stars being more metal-rich. This is consistent with those stars being younger. Bottom right: $\log(R'_{\text{HK}})$ vs. R_* . This plot shows that as activity increases to the right, most stellar radii are near $1.0 R_{\odot}$.

Table 1
Gaussian Fit Parameters

Property Bin	Amplitude	Mean	Sigma	Amplitude	Mean	Sigma	Chi-squared	Reduced Chi-Squared
Full Sample (893)	111.5	-5.167	0.143	24.73	-4.691	0.242	500.19	20.84
$T_{\text{eff}} > 6000$	30.75	-5.25	0.14	309.30	11.46
$5400 < T_{\text{eff}} < 6000$	56.89	-5.12	0.14	825.83	30.59
$T_{\text{eff}} < 5400$	7.26	-4.92	0.44	180.21	6.67
$[\text{Fe}/\text{H}] < -0.1$	25.18	-5.15	0.16	119.22	4.42
$-0.1 < [\text{Fe}/\text{H}] < 0.1$	35.03	-5.14	0.18	796.18	29.49
$[\text{Fe}/\text{H}] > 0.1$	26.83	-5.13	0.22	507.50	18.80
$R_* > 1.2$	72.28	-5.22	0.11	494.04	18.30
$0.9 < R_* < 1.2$	35.02	-5.07	-0.13	436.10	16.15
$R_* < 0.9$	9.08	-4.78	0.31	267.61	9.91
$T_{\text{eff}} > 6000$	27.00	-5.25	0.12	4.94	-5.32	-0.37	248.36	10.35
$5400 < T_{\text{eff}} < 6000$	62.91	-5.18	-0.18	-28.45	-5.34	0.11	697.72	29.07
$T_{\text{eff}} < 5400$	7.26	-4.92	0.44	1.00	-5.70	0.03	180.21	7.51
$[\text{Fe}/\text{H}] < -0.1$	23.87	-5.15	-0.14	1.87	-5.06	-0.58	102.02	4.25
$-0.1 < [\text{Fe}/\text{H}] < 0.1$	14.38	-7.06	0.05	35.03	-5.14	-0.18	796.18	33.17
$[\text{Fe}/\text{H}] > 0.1$	10.48	-4.86	0.37	24.01	-5.18	0.13	92.77	3.87
$R_* > 1.2$	65.36	-5.22	0.10	9.78	-5.34	0.27	294.67	12.28
$0.9 < R_* < 1.2$	7.84	-4.86	0.28	31.62	-5.09	0.10	198.27	8.26
$R_* < 0.9$

period and chromospheric activity is present, we expect stars with similar stellar temperature to have a smooth function with rotation period. Instead, in the left panel, we see a large amount of scatter at every temperature where stars are less active. By analyzing only stars that rank as (David et al. 2021) highly reliable from the CKS-HK rotation sample, the temperature, rotation, and activity relation are clarified (Figure 9, right panel). A correlation between stellar surface temperature,

$\log(R'_{\text{HK}})$ and rotation period is now visible. Metcalfe et al. (2016) showed a similar relationship (their Figure 1), noting the different slopes for different spectral types and lack of long rotation period stars for solar-type stars. We do not yet filter on stellar properties by removing subgiants, but few subgiants have definitive rotation periods because they have fewer surface inhomogeneities. By focusing solely on the most well-determined rotation periods, and validated $\log(R'_{\text{HK}})$ values, we

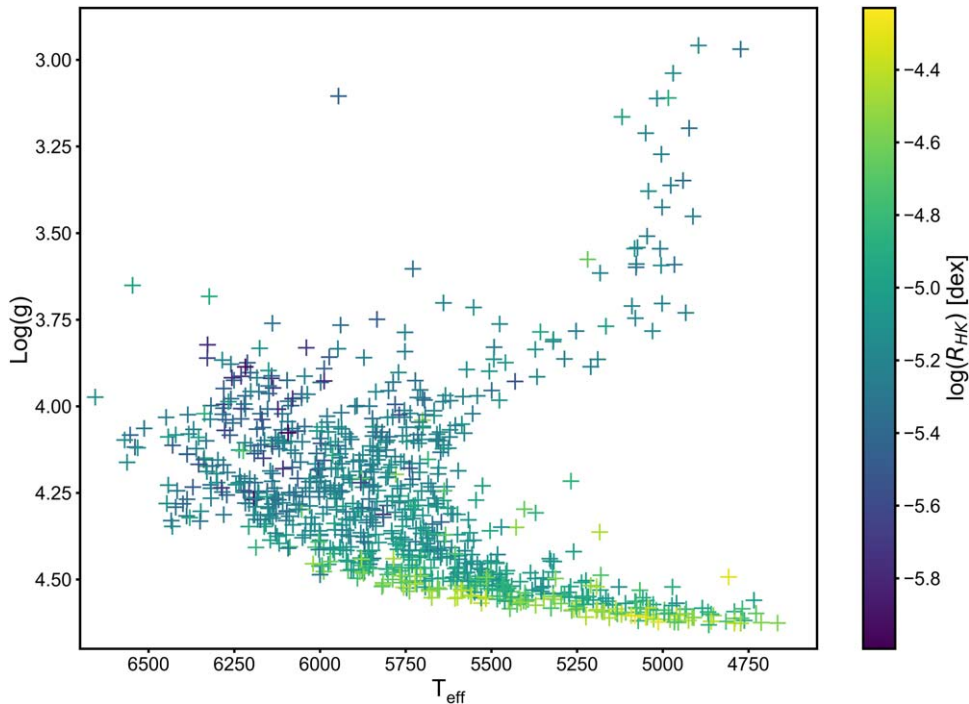


Figure 8. Stellar surface gravity is plotted as a function of stellar effective surface temperature for the CKS-HK stellar sample of 879 stars. The color bar indicates $\log(R'_{HK})$ with yellow as more active and purple as less active. The giant branch moves from the center to the upper right of the plot. The most active stars (yellow) are cool dwarfs that make up the lower envelope of the main sequence. From CKS-Gaia (Fulton & Petigura 2018), the typical errors on T_{eff} and $\log(g)$ are 60 K and 0.01 dex, respectively. We use the calibration error of 0.02 as the uncertainty on $\log(R'_{HK})$.

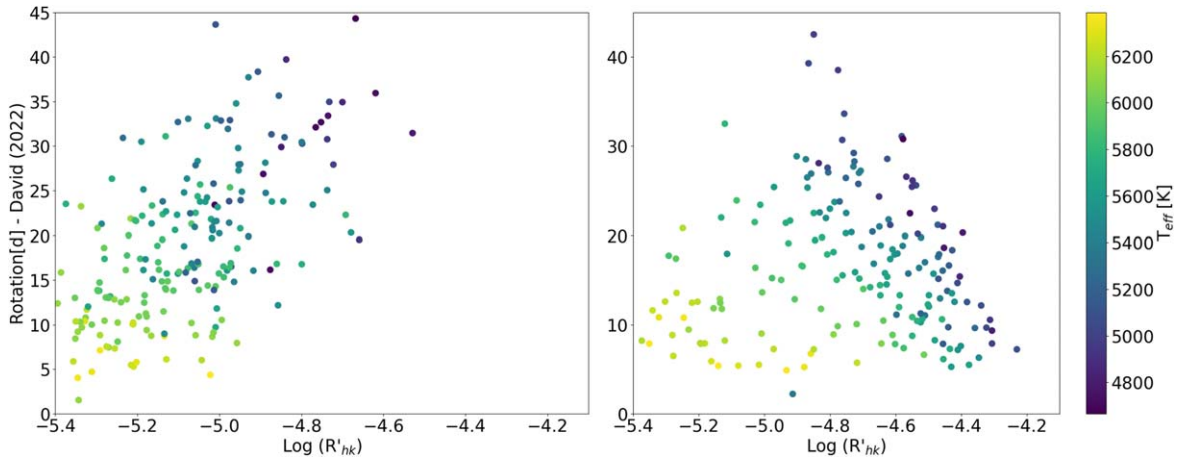


Figure 9. Left panel: Kepler rotation periods are plotted as a function of $\log(R'_{HK})$ and all rotation periods from David et al. (2021) are included. Right: only grade 3 rotation periods from David et al. (2021) are plotted. In the left and right panel, 215 and 184 stars from the CKS-HK rotation sample are plotted, respectively. Recovering stellar rotation periods with single-epoch Ca II H and K measurements is challenging because $\log(R'_{HK})$ values for a given star naturally vary. Our Sun’s 11 yr stellar activity cycle, which changes the average $\log(R'_{HK})$ value preserves the 27 day rotation period. The colors denote stellar surface temperature with cooler stars having darker shades. We expect rotation period to be related to activity within a given temperature bin.

can make further definitive statements about rotation periods and the stellar properties provided by the HIRES spectra in the CKS-HK rotation sample, which we do in Section 3.3.

3.2.2. Photometric versus Activity Derived Rotation Periods

Recovering stellar rotation periods with single-epoch Ca II H and K measurements is challenging because $\log(R'_{HK})$ values for a given star naturally vary, similar to our Sun’s 11 yr stellar activity cycle, changing the average $\log(R'_{HK})$ value while preserving the 27 day rotation period. Noyes et al. (1984) used a few tens of stars to create relations between Rossby

number, convective turnover time, and rotation period, but relied on average S -values of stars that had been collected over decades, which effectively averaged out the stellar activity cycles $\log(R'_{HK})$ values. The long-term nature of that data set makes it very valuable for analyzing stellar activity cycles as producing accurate long-term averages. We will utilize a larger number of stars with single epochs of activity measurements, and rely upon the larger number offset the lack of time series when we calculate rotation periods using the Mamajek & Hillenbrand (2008) activity-period relations, which are very similar to Noyes et al. (1984), and compare them with photometric rotation periods from Kepler.

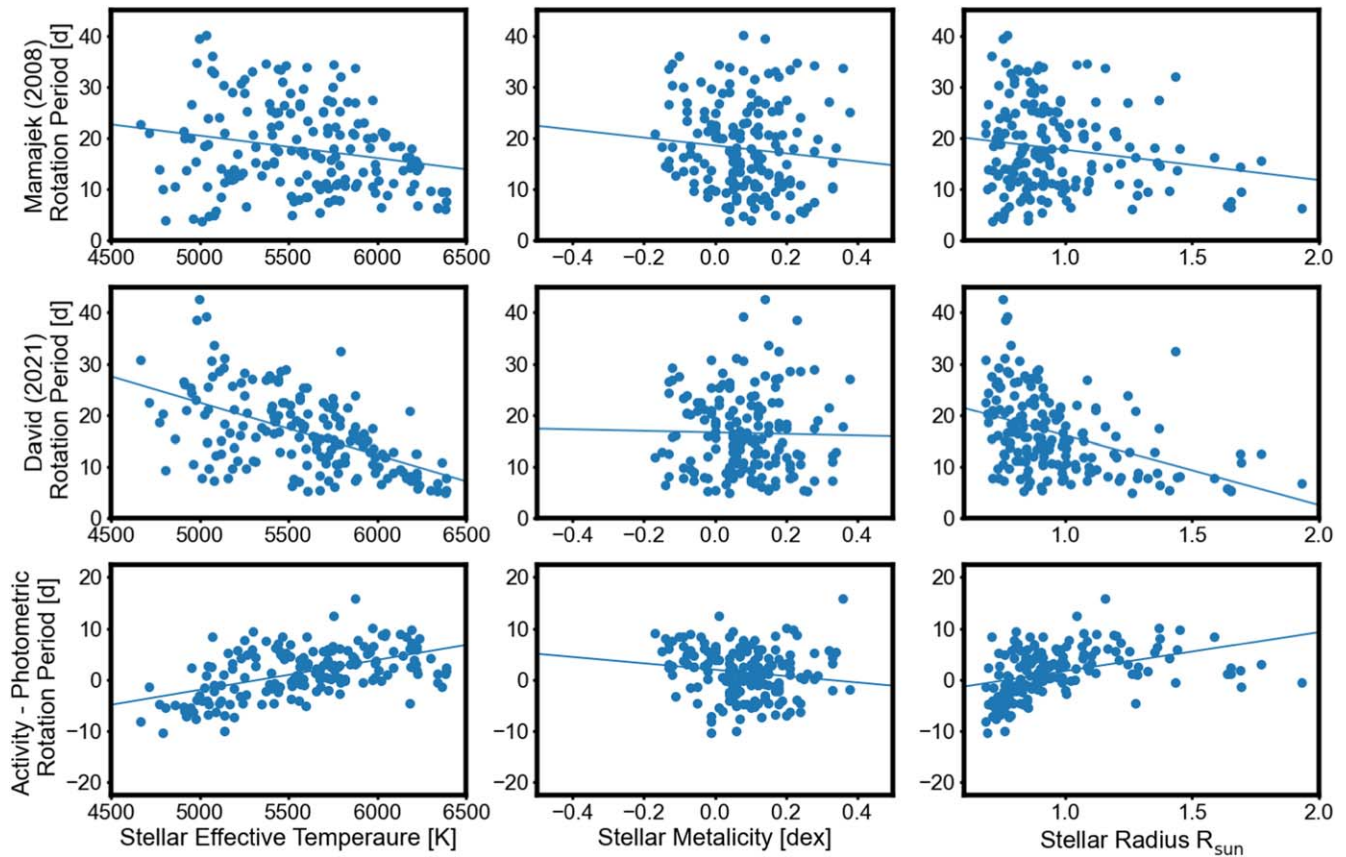


Figure 10. The top row shows the Mamajek & Hillenbrand (2008) rotation periods, derived from S -values as a function of T_{eff} , $[\text{Fe}/\text{H}]$ and stellar radius from left to right. Each vertical column is the same in all rows. The second column shows the David et al. (2021) rotation periods with very-reliable grade. The bottom row shows the difference between activity derived rotation periods and the photometric rotation periods as a function of each stellar property for for each plot for 173 stars from the CKS-HK rotation sample with $\log(g) > 4.0$ and grade 3 rotation periods. The rotation period uncertainties are 10%.

3.3. Rotation Period and Fundamental Stellar Properties

3.3.1. Overview

To explain inconsistencies between stellar spindown models and observations of rotation periods for stars older than 1 Gyr, van Saders et al. (2016) developed theoretical relations that better describe spin down than empirical relations (Skumanich 1972). van Saders et al. (2016) showed that asteroseismically determined rotation periods (Hall et al. 2021) align with their theory of WMB and can reliably predict stellar rotation periods for stars older than 1 Gyr.

The Van Sanders conclusions are reinforced by the work of Metcalfe & Egeland (2019), who provide additional observational evidence that there exists a transition phase for stellar spindown that occurs in middle ages stars that leads to a breakdown of the previous spin–age relation for stars older than 1 Gyr. They show that the consistency between gyrochronology ages and ages determined with chromospheric activity break down near a value of $\log(R'_{\text{HK}})$ of -4.95 . In analyzing the rotation periods and T_{eff} , David et al. (2022) used Kepler derived rotation periods to solidify the conclusions of van Saders et al. (2016) by showing that stars older than a few gigayears do not spin down beyond a certain point stalling to populate the Rossby Ridge.

3.3.2. Rotation Period, T_{eff} , $[\text{Fe}/\text{H}]$, and R_*

We use the CKS-Gaia precise stellar parameters, our $\log(R'_{\text{HK}})$ activity measurements, the activity-derived rotation

periods, and photometric rotation periods to examine rotation-activity relationships. In Figure 10 we plot rotation periods derived from $\log(R'_{\text{HK}})$ using the Mamajek & Hillenbrand (2008) equations, the Kepler photometric rotation periods from David et al. (2021), and the difference in those values versus stellar properties for each star. We select only the grade 3, highly reliable, rotation periods from David et al. (2021), and we remove subgiants by restricting the $\log(g)$ to be greater than 4.1 leaving 173 stars. Using this highly selective set of rotation periods, we calculate the difference between Kepler photometric rotation period and the activity derived rotation periods. For each panel in Figure 10, we fit a linear trend to the data to assess trends in each stellar property. We checked for evidence that the S/N of the S -value measurements affects the S -values themselves and found none, reducing the chance that a systematic error is occurring due to low S/N.

In the T_{eff} versus P_{rot} plots (Figure 10, left column), we see the expected trend, hotter stars rotate faster, but the slope between the two rotation determinations is quite strong. If the difference plot for activity-derived rotation periods and photometric rotation periods showed a flat slope, then both determination methods would agree. Instead, the activity-derived relation overpredicts rotation periods for cool stars and underpredicts rotation periods for hotter stars. The main result of the stellar property and rotation period analysis is that the relations for determining rotation period work very well for solar-type stars, but less well as stars diverge from solar T_{eff} . This reflects the bias toward solar-type stars used in the

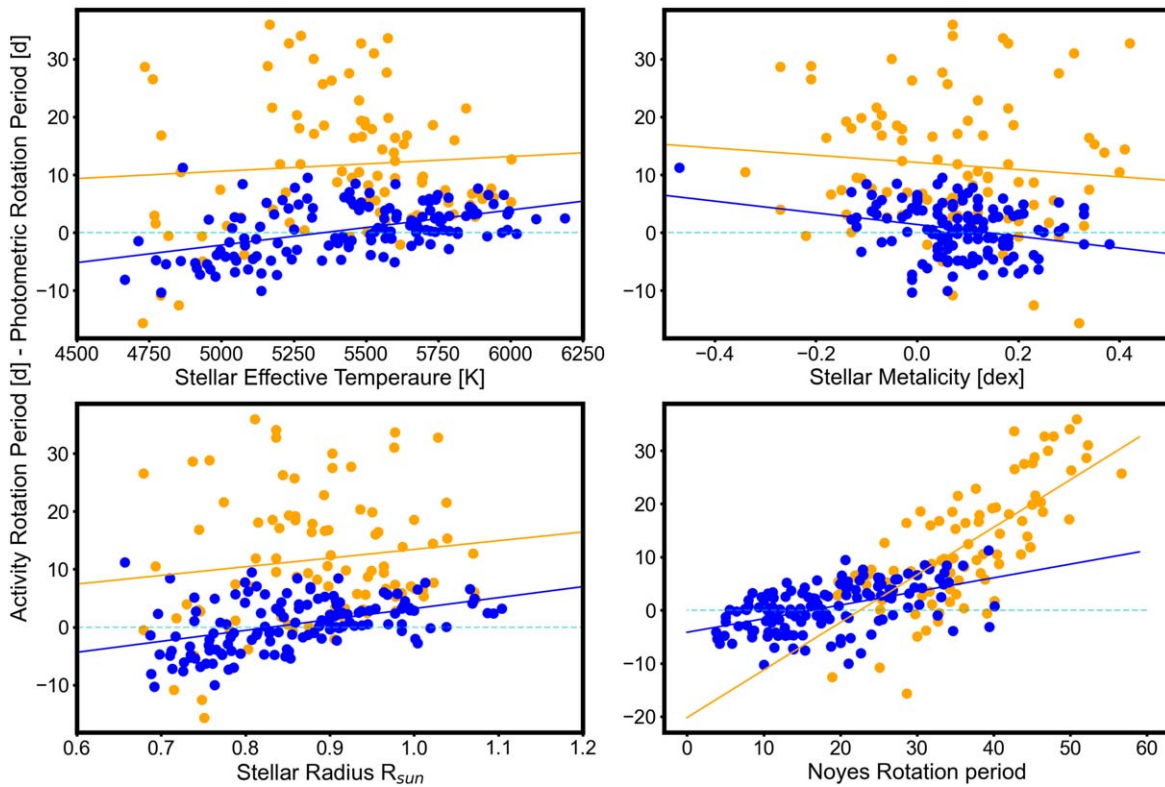


Figure 11. The difference between photometric and activity derived rotation periods are plotted on the y-axis of each plot for 130 stars from the CKS-HK rotation sample with $\log(g) > 4.4$ and have rotation periods with grade 2, reliable (orange points) or grade 3, high reliable (blue points). The rotation period uncertainties are 10%. Top left: the grade 2 rotation periods are far more discrepant than the grade 3 rotation periods and both show the same modest correlation with T_{eff} . Top right: the grade 2 rotation periods show a larger variation in metallicity than those with grade 3. Bottom right: the grade 2 rotation periods show a strong correlation when plotted against the activity derived periods. This shows that for stars with a clear but not strong photometric rotation period (grade 2), the discrepancy between the two methods of obtaining the rotation period is more than 30% for periods beyond 40 days. If the photometric rotation period is very clear, the agreement is much better, but the photometric rotation periods do not extend beyond 40 days. Bottom left: stellar radius shows a modest slope, meaning there is a systematic error in rotation period determinations from activity metrics that is linear with R_* .

creation of past activity-period relationships, and motivates the development of the WMB theory of stellar spindown.

When considering $[\text{Fe}/\text{H}]$ (Figure 10, center column), we see a linear correlation with metallicity for the activity derived periods, but no trend for the photometric periods. This disconnect may reveal the bias of Mt. Wilson survey toward solar metallicity stars. The negative trend with stellar metallicity shows that more metal-rich stars have rotation periods that are underpredicted by activity. Contrast this with metal-poor stars showing rotation periods that are overpredicted compared to the photometric rotation periods. Amard & Matt (2020) and Avallone et al. (2022) both studied the influence of metallicity on rotation periods. The former used theoretical models to conclude that stars of the same mass but with metal-poor versus solar metallicity rotate faster and have a higher Rossby number resulting from the change of the depth of the convective zone. The latter measured rotation periods in TESS and Kepler light curves that do not show a statistically significant relationship between metallicity and rotation period. These analyses could be more definitive with larger samples of stars that have more extreme metallicities than we present.

In Figure 10, right column, the stellar radii are plotted against the activity-determined, photometric rotation period, and the difference between the two. We see correlations in the two determinations of rotation periods that suggest a faster rotation period for larger stars. The more numerous solar-type

stars and sparse number of larger stars makes the conclusion ambiguous.

In Figure 11 we plot only the difference panels from the previous figure, and we now include grade 2 (reliable, orange points) and grade 3 (highly reliable, blue points) rotation period labels. The differences between the activity-derived and photometric rotation periods are more pronounced for those that are deemed less reliably determined. This is likely explained by the lower-precision ground-based data, compared to Kepler data, that was used to generate the rotation-activity relations from Noyes et al. (1984) and Mamajek & Hillenbrand (2008).

3.3.3. Rossby Number and Chromospheric Activity

Recent work by David et al. (2022) used CKS-Gaia stellar properties and Kepler photometric rotation periods to reveal the Rossby Ridge, a clustering of stars in T_{eff} versus rotation period space that supports the theory of WMB. We use the CKS-HK rotation sample and our $\log(R'_{\text{HK}})$ measurements to determine if chromospheric activity supports the presence of a Rossby Ridge. First we examine our $\log(R'_{\text{HK}})$ values by comparing to the population of main-sequence stars used by Mamajek & Hillenbrand (2008).

The theoretical connection between chromospheric activity and stellar rotation is via the Rossby number, the ratio of the rotation period to the convective turnover time. By calculating

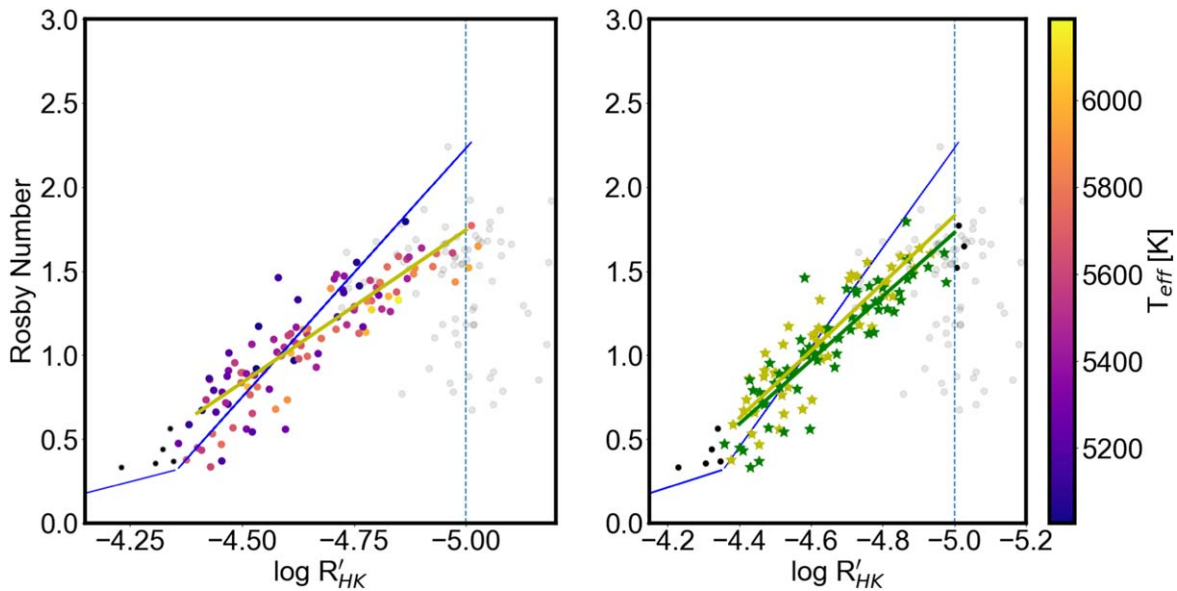


Figure 12. Left panel: the CKS-HK rotation sample is shown in relation to their $\log(R'_{\text{HK}})$ values and Rossby numbers as determined by the Kepler rotation period divided by the convective turnover time as defined in Noyes et al. (1984), Equation (4). The best-fit from Mamajek & Hillenbrand (2008), Equation (5) is overplotted in blue. T_{eff} is less than 6250 K, and $\log(g)$ is required to be greater than 4.4, matching those cuts in that paper. The vertical line is the value of -5.0 , shown to be the limit of the rotation-activity relations. The colors scale is stellar surface temperature. Right panel: the two colors represent $[\text{Fe}/\text{H}]$ values divided at the median of the distribution, $[\text{Fe}/\text{H}] = +0.09$. The yellow and green fits to the lower and higher metallicity data are consistent with each other, showing that the impact of metallicity on this relation is weak in the range of $[\text{Fe}/\text{H}]: [-0.3, +0.3]$. The grayed-out data points are the CKS-HK stellar sample that have grade 0 or 1 stellar rotation periods and are not used in the fits.

the Rossby number using the Kepler rotation periods, we can compare $\log(R'_{\text{HK}})$ and Rossby number (Mamajek & Hillenbrand 2008, their Figure 7). We focus our analysis in the active regime ($-5.0 \leq \log(R'_{\text{HK}}) \leq -4.3$), since we lack a sufficient number of stars in the very-active regime ($\log(R'_{\text{HK}}) \leq -4.3$). In Figure 12 we plot $\log(R'_{\text{HK}})$ versus the Rossby number for our CKS-Gaia stellar sample, using 107 “very-reliable,” photometric rotation periods (grade 3). The temperature range has been limited from 5000–6200 K, and the $\log(g)$ must be greater than 4.4, focusing on main-sequence stars and matching Mamajek & Hillenbrand (2008). Only data in the bounds of $\log(R'_{\text{HK}})$ between -4.3 and -5.0 are used in the fit. The gray data are CKS-HK stars with unreliable, indistinct, or “reliable” rotation periods, flags of 0, 1, or 2 from David et al. (2021).

To assess subtleties in Figure 12, we split the sample in metallicity to reveal that $[\text{Fe}/\text{H}]$ does not play a strong role in the relationship between Rossby number and $\log(R'_{\text{HK}})$. We show the same data in both panels of Figure 12, with the best-fit from Mamajek & Hillenbrand (2008) in blue. The color bar describes the T_{eff} of the sample in the left panel. A vertical dotted line at $\log(R'_{\text{HK}}) = -5.0$ identifies values where we expect a breakdown in the standard activity-rotation relations (Metcalf & Egeland 2019). By fitting a line to the data in the left panel, we find a fit with a shallower, but similar slope compared to Mamajek & Hillenbrand (2008). The right panel shows a similar version with the stellar metallicity highlighted as two distinct colors divided at the median value of those plotted, $+0.09$. We find a very similar slope when fitting the lower-metallicity and higher-metallicity halves of the data separately, suggesting that metallicity does not play a strong role in this relationship, at least in the range of $[-0.2$ to $+0.3]$.

Figure 12 reveals an upper limit of 1.75 on the Rossby number. Theoretical work suggests that the critical Rossby number is 2.0 or 2.16, higher than any of our target stars. This

is explained by our restrictions on rotation period quality and the gravity cutoff of 4.4.

David et al. (2022) provided evidence in support of the van Saders et al. (2016) theory of WMB via the identification of the long-period pile-up in the temperature-rotation plane that results from magnetic braking. By using the CKS-Gaia sample and controlling for the quality of the rotation periods, the Rossby Ridge is identifiable. We rely on the same robust stellar properties from the CKS-Gaia sample and strictly vetted rotation periods to further confirm the theory of WMB.

We replicate the temperature versus rotation period plot from David et al. (2022) and add chromospheric activity data in the form of rotation periods derived from $\log(R'_{\text{HK}})$ values (Figure 13). We color-code the stars for which the activity derived rotation period is larger than the photometric rotation period by more than 30%. With the standard uncertainty of the photometric rotation periods of 10% according to David et al. (2022), the choice of 30% corresponds to a 3σ discrepancy between rotation period determination methods. For all stars in the T_{eff} range of 5850–6250 K, the photometric rotation period is smaller than the activity derived period. We find that 79% of the stars in the trapezoid region have overpredicted rotation periods of more than 30%. This discrepancy points to the disconnect between the rotation period and magnetic field of a star, as stars reach a few gigayears old, as described by the theory of WMB. Masuda (2022) pointed out that the pile-up of stars in the P_{rot} versus T_{eff} plane is also affected by the decrease in the photometric amplitude of the rotation signal and that the pile-up may in fact be at longer periods but is currently below our detection limits.

To further explore the T_{eff} and rotation period plane, we change the color-code of $\log(R'_{\text{HK}})$ values in Figure 14 and search for a connection between the $\log(R'_{\text{HK}})$ values and the Rossby Ridge. By dividing the $\log(R'_{\text{HK}})$ values at -4.8 and -5.1 , we can identify stars that lie along the Rossby Ridge. There are 3/103 stars with $\log(R'_{\text{HK}}) > -4.80$, 34/103 between

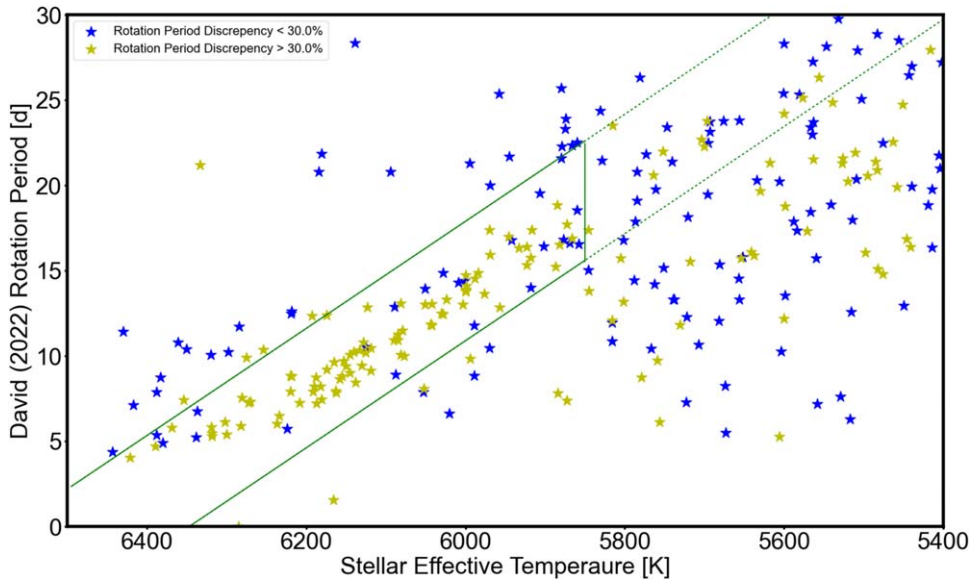


Figure 13. The temperature vs. rotation period plane similar to David et al. (2022, their Figure 4). Each symbol represents a star from the CKS-HK rotation period sample with grade 2 or 3 rotation period and $\log(g) > 4.0$. Blue symbols identify stars that show agreement between their photometric and activity derived rotation periods to better than 30%. Yellow data points show discrepancy larger than 30%. Large discrepancy points to a disassociation of the stellar spindown with age, consistent with the theory of weakened magnetic braking. We extend the trapezoid defined in David et al. (2022) to 5600 K, but find no evidence in the $\log(R'_{\text{HK}})$ data that inform the breakdown of the Ridge into that range of T_{eff} .

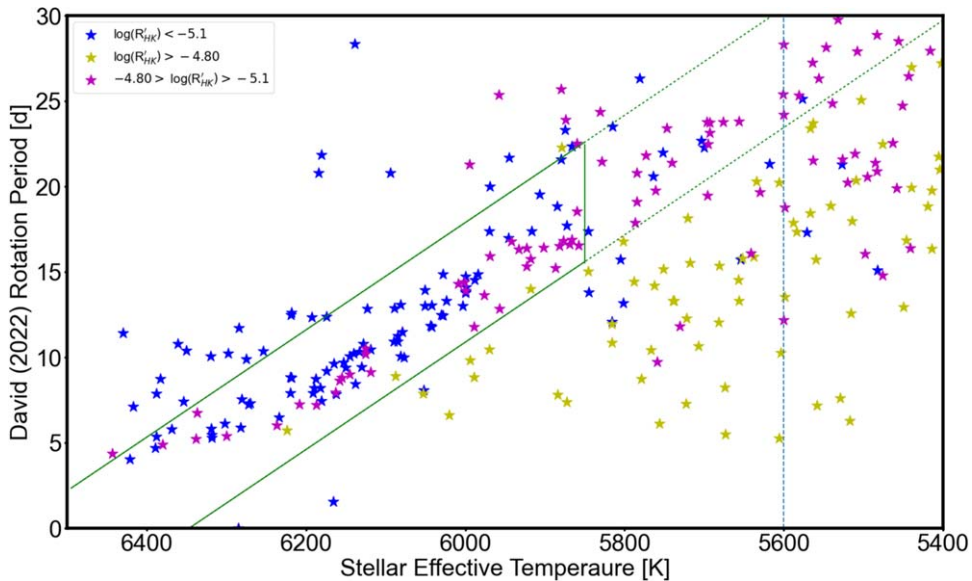


Figure 14. The T_{eff} vs. rotation period plane similar to David et al. (2022, their Figure 4). Each symbol represents a star from the CKS-HK rotation period sample with grade 2 or 3 rotation period and $\log(g) > 4.4$. Blue symbols are least active $\log(R'_{\text{HK}}) < -5.1$, representing inactive stars. Yellow symbols have $\log(R'_{\text{HK}}) > -4.80$, representing the active stars. Yellow symbols are within 0.15 of the critical value of $\log(R'_{\text{HK}}) = -4.95$, where we expect the traditional spindown relations to break down in favor of the relations best described by weakened magnetic braking.

$\log(R'_{\text{HK}})$ of -4.80 and -5.10 and 66 stars in the least active category of $\log(R'_{\text{HK}}) < -5.10$. We expect stars of a certain T_{eff} , say 6000 K, to slowly spin down with age but to not change temperature while on the main sequence. If we had a population of more quickly rotating stars that populated the area below the trapezoid, we could likely see the most active stars with the fastest rotation periods, and stars with ever decreasing activity as they approach the Rossby Ridge. Our population of stars from 5850–6200 K has insufficient younger and more active stars to see the type of behavior that is seen in surveys with larger numbers of stars, such as McQuillan et al. (2014).

We extend the trapezoid defined in David et al. (2022) from 5850–5600 K and find tentative evidence in the $\log(R'_{\text{HK}})$ data that indicates Rossby Ridge projects into cooler ranges of T_{eff} . These stars have thicker convective zones, spend longer on the main sequence, and take longer to spin down. These larger parameter spaces, and longer time spans in stellar evolution are a barrier to theoretical studies attempting to explain spindown for broader stellar populations. The conclusions by Masuda (2022) regarding the amplitudes of stellar rotation signals are even more relevant for this range of T_{eff} since these stars are inherently fainter,

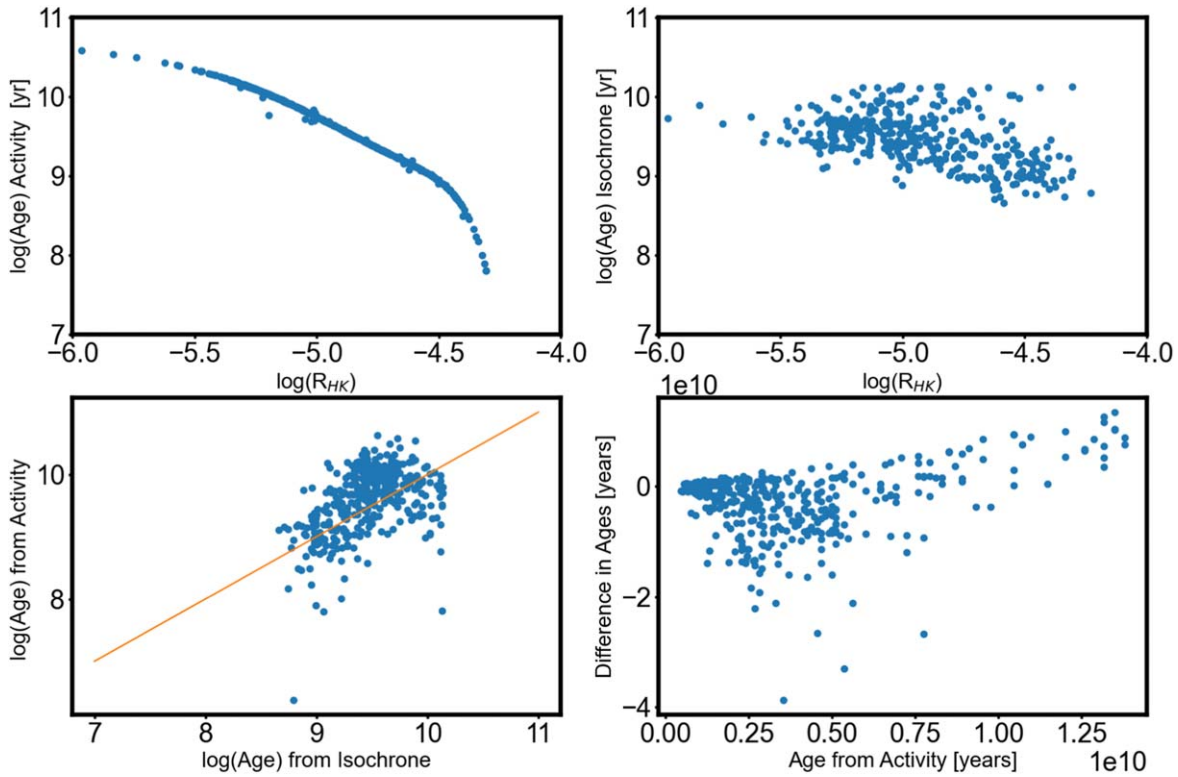


Figure 15. We explore the age vs. activity relationship with these four panels. Top left: the predicted rotation period determined the $\log(R'_{HK})$ value of the star. Top right: the isochronal age from David et al. (2021) or CKS-Gaia as a function of the chromospheric activity. Bottom left: the isochronal age compared to the activity derived age and the one-to-one line overplotted. Bottom right: the difference between the two age determinations as a function of the isochronal age. Note this plot is in units of years, and the others are in log (age).

Table 2
Activity Metrics and Derived Values

Starname (KOI)	S -value	$\log(R'_{HK})$	S/N per pixel	P_{Rot} Activity(d)	$\log(\text{Age})$ Activity (yr)	Quality	Quality Flag	P_{Rot} Phot(d)	P_{Rot} Flag
K00001	0.145	-5.101	8	30.1	9.90	0	bad seeing	0.0	1
K00002	0.128	-5.247	11	6.9	10.09	1	ok	0.0	1
K00006	0.140	-5.103	19	8.5	9.91	1	ok	0.0	0
K00007	0.141	-5.136	27	30.9	9.95	1	ok	0.0	1
K00008	0.202	-4.779	14	16.6	9.40	1	ok	0.0	0
K00010	0.127	-5.270	19	16.8	10.12	1	ok	7.5	2
K00017	0.134	-5.202	10	41.8	10.04	1	ok	0.0	1
K00018	0.125	-5.289	19	10.9	10.14	1	ok	0.0	1
K00020	0.136	-5.178	21	27.3	10.00	1	ok	0.0	1
K00022	0.135	-5.190	17	29.5	10.02	1	ok	0.0	1

(This table is available in its entirety in machine-readable form.)

further clouding our ability to draw conclusions for these stars.

3.4. Ages and Chromospheric Activity

The works of van Saders et al. (2016), David et al. (2022), and Metcalfe & Egeland (2019) attempted to find a relationship between age, activity, and rotation, similar to Noyes et al. (1984), but with modern tools. Noyes et al. (1984) used rotation periods and a few assumptions about stellar structure. By examining two stars of similar T_{eff} and near the Kraft Break, Metcalfe & Egeland (2019) revealed the age–activity relation discontinuity, near $\log(R'_{HK})$ of -4.95 . For more active stars, the relationship between chromospheric ages and gyrochronology ages agree, but once

stars’ activity decreases beyond $\log(R'_{HK})$ of -4.95 , the age determinations diverge.

Figure 15 shows our two age metrics as function of $\log(R'_{HK})$ in the two top panels. In the two bottom panels, the isochronal age is compared to the activity-derived age, and to the difference in the two age metrics for each star, in the left and right panels, respectively.

Broadly speaking, the chromospheric ages are overpredicted compared to the isochrone ages. Given our evidence in favor of WMB, we expect the activity-age determinations to perform poorly for stars older than 1 Gyr. However, the mismatch in ages between the youngest, most active, stars is unexpected. The S -values, $\log(R'_{HK})$ values, rotation periods and activity derived ages for the CKS-HK star sample are collected in Table 2.

3.5. The Most Inactive Stars: Overview

Stars that mimic the activity of the Sun during its persistent minimum in the 17th century have been sought in an attempt to solidify the solar-stellar connection. Duncan et al. (1991) collected 18 yr of S -value time series with the Mt. Wilson H&K Activity project providing many examples of stars with solar-like stellar activity cycles (Baliunas et al. 1995), and several candidates for stars in low activity states. These stars were chosen as bright, Sun-like stars, but without the vigor of spectroscopic stellar classification that we have today. One method for identifying a star in Maunder minimum-like state (or magnetic minimum) is to look for a decrease in the S -values over time or a transition from a stellar cycle into a noncycling state. Several candidate Maunder minimum stars from the Mt. Wilson survey data alone were identified, though none has stood up to further scrutiny (Wright 2004) without additional data. Continued efforts to add modern data to the Mt. Wilson HK project's time-series data have identified several MM candidates.

With the addition of California Planet Search $\log(R'_{\text{HK}})$ data, Shah et al. (2018) identified HD 4915 as a candidate for being in an activity minimum, but recent data showed the activity minimum is ending. Another analysis of the Mt. Wilson HK project plus CPS data (Wright et al. 2004; Isaacson & Fischer 2010) extended the observing baseline for 59 stars from two to five decades.

Baum et al. (2022) curated the various data sets and identified HD 166620 as a star that was in a previously cycling state and is now in a noncycling low-activity state. An extended effort has confirmed HD 166620 as a true MM star (Luhn et al. 2022) using photometry and critically timed S -value measurements. In that study, intraseasonal variability was considered a more useful diagnostic of an MM state than instantaneous measurements that are anomalously low.

Searching for MM stars by analyzing decades of time-series data is laborious and time consuming so other methods for identifying stars in activity minima have been explored. Surveys like the Hipparcos Mission (Perryman et al. 1997) made the identification of outliers more robust with precise measurements of parallax. The distance can be combined with spectral surveys that provide precise stellar surface gravities and metallicities (Wright 2004; Fulton & Petigura 2018; Rosenthal et al. 2021). Naturally, Gaia now provides precise parallax measurements for all stars down to $V \sim 19$. The parallaxes can help to disentangle inactive main-sequence stars from evolved stars that are naturally inactive. The Gaia spectral measurements of the Calcium infrared triplet may enable statistical searches for inactive stars based on a small number of measurements for each star.

We can use the CKS-HK sample of stars to identify the least active stars and present candidates of stars in magnetic minima.

3.5.1. Identifying Stars in States of Magnetic Minima via Stellar Properties

The discussion on what constitutes an MM candidate has become more nuanced as our ability more precisely measure the fundamental stellar parameters of surface gravity, effective temperature, and metallicity have improved. We attempt to identify stars in an MM state, using a variety of methods including those of Wright et al. (2004) and Saar (2011). Henry et al. (1996) claimed that using a single $\log(R'_{\text{HK}})$ value to

identify quiet stars, for example, with a $\log(R'_{\text{HK}}) < -5.1$, is insufficient. Using T_{eff} , $\log(g)$, and $[\text{Fe}/\text{H}]$ is required (Saar 2011), and multiepoch spectroscopy is ideal (Baum et al. 2022). The CKS-Gaia stellar properties catalog enables a detailed study of activity, temperature, surface gravity, and metallicity in the search for the MM stars using single-epoch spectra.

The reliability of the metric $\log(R'_{\text{HK}})$ depends on the inputs as defined in Noyes et al. (1984). Modern studies have created new variations on $\log(R'_{\text{HK}})$, such as Hall et al. (2007), who prefer to use F_{HK} and ΔF_{HK} . This metric provides a different but related way for obtaining a minimum activity level. Improvements in the calculation or $\log(R'_{\text{HK}})$ or of the bolometric corrections could be useful in identifying the least active stars. Mittag et al. (2013) created the $\log(R_{\text{HK}}^{\dagger})$ metric, which separates the flux in the H&K lines into the basal, photospheric, and chromospheric components to create a metric at which the minimum activity level is 0 by definition. Saar (2011) required MM stars to have a minimum activity level, but did not assume it is based only on T_{eff} , which was assumed by Noyes et al. (1984). This leads to a minimum level of activity that might indicate MM stars vary as a function of $V \sin(i)$, $\log(g)$, and $[\text{Fe}/\text{H}]$ as well as T_{eff} . Additionally, it requires knowing something about the longer-term variation, which can be variation of S -value over time (Saar 2011), or photometry (Hall et al. 2007) or X-rays (Judge & Saar 2007). Judge & Saar (2007) claimed that an MM star can only be confirmed if we know something about the X-ray flux, which can only be produced by a stellar dynamo.

We define the height above the main sequence using the Wright (2004) relation and search for stars that are both inactive, $\log(R'_{\text{HK}})$ less than -5.1 , and near or below the main sequence. To identify interesting candidates, we focus on the stellar temperature range of 4700–5500 K, where the main-sequence population and subgiant populations are well separated. Knowing that MM stars are rare, we are looking for outliers from the populations. In Figure 16, we identify no stars in the coolest bin that are MM candidates. In the 5500–6000 K bin, we see a set of stars, the most extreme of which may be an MM candidate. The best candidate in the 5500–6000 K bin is KOI-1531. There is a population of stars in the lower right quadrants for the temperatures 6000–6500 K. There are no outliers, but rather stars that naturally fall into the bottom-left box. We expect this because near the Kraft Break at T_{eff} of 6250 K, stars become fully radiative, and the sort of activity that we are probing is not viable through the same physical mechanisms as for cooler stars.

We highlight cool stars that lie far below the main sequence in a temperature–magnitude diagram (Figure 17). There are three stars that are more than 0.4 magnitude below the main sequence, as defined by Wright (2004) and are cooler than 6250 K, the Kraft Break. They are KOI-1531, KOI-4144, and KOI-5236. KOI-5236 has a planet with a period greater than 500d, and maybe false-positive planet candidate according to Community Follow-up Program (CFOP; Gautier et al. 2010). It has $T_{\text{eff}} = 6100$ K, $\log(g) = 4.41$, and $\log(R'_{\text{HK}}) = -5.365$. It is very inactive and has a $1''9$ companion, but no detection of a secondary star in the spectrum. The nearby star makes the likelihood of the star being an MM star less certain. KOI-4144 has T_{eff} of 6000 K, $\log(g) = 4.49$, especially large RMS3 value from Kepler (Christiansen et al. 2012), distance of 860 pc. KOI-1531 is the furthest below the main sequence, and it has a

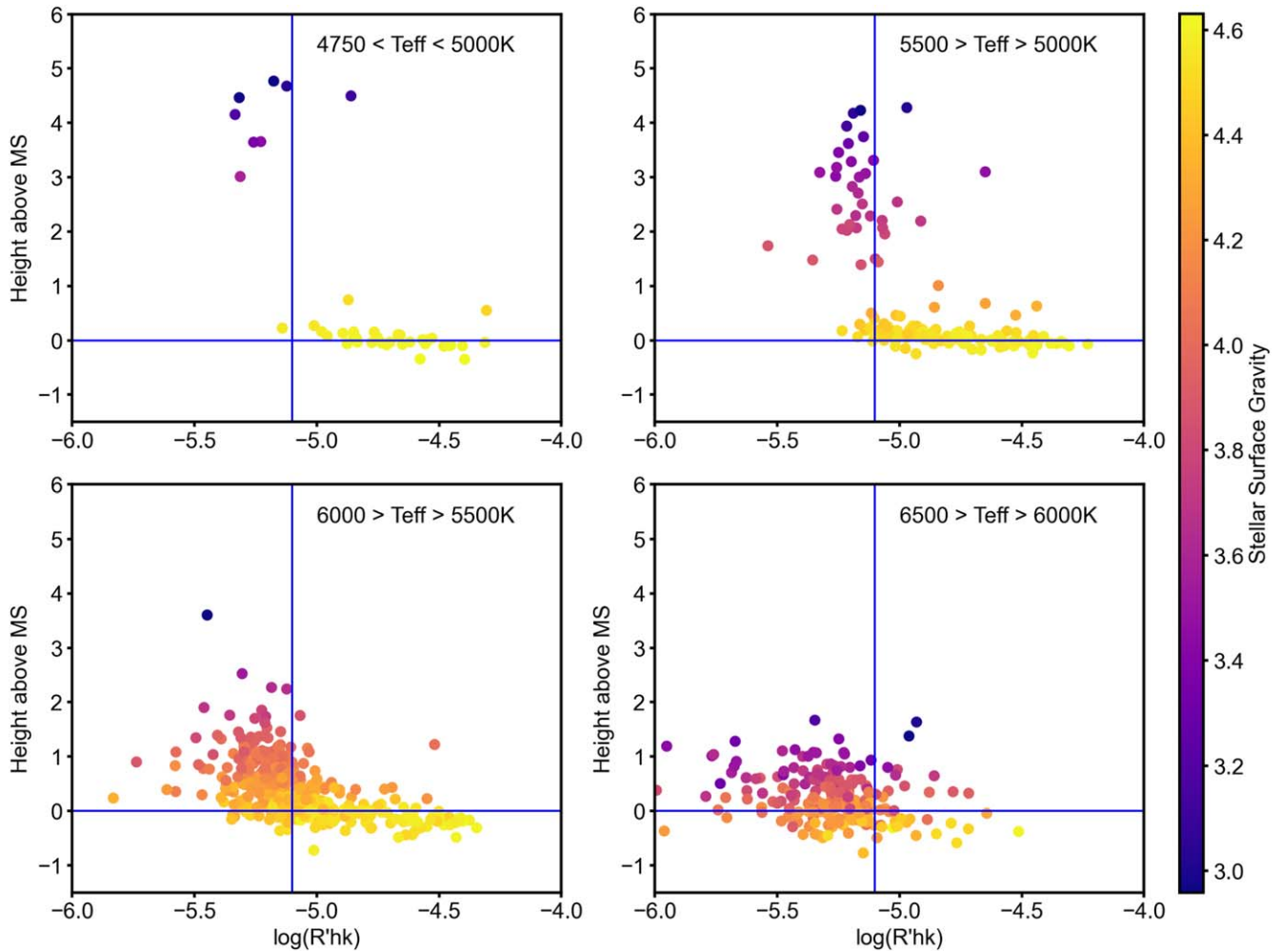


Figure 16. Examining delta magnitude above the main sequence (Wright 2004) vs. $\log(R'_{\text{HK}})$, we expect stars that are experiencing magnetic activity minima to be in the bottom-left quadrant of these plots. Stars that populate the upper-left quadrant tend to be subgiants with large radii that are likely have their magnetic fields decoupled from their convective zones. The vertical line at $\log(R'_{\text{HK}}) = -5.1$ is an arbitrary but reasonable division between active and inactive stars (Henry et al. 1996). Saar (2011) stated that it is not a good cutoff for MM star consideration because it was made before Hipparcos helped define the evolutionary state of a large sample of stars. We focus on main-sequence stars with $T_{\text{eff}} < 5500$ K because we do not expect them to populate very inactive regime, except in extreme circumstances, such as Maunder minimum stars.

near Sun-like T_{eff} , and $\log(g)$ with $\log(R'_{\text{HK}}) = -5.012$. It has a photometric rotation period from Angus et al. (2018) of 23 days and an activity rotation period of 34 days. This 30% discrepancy mismatch between the photometric and activity rotation periods is supportive of the theory of WMB. If this is the case, the star is old and inactive, but still has the rotation period of a younger star.

Henry et al. (1996) states that stars with $\log(R'_{\text{HK}}) \leq -5.1$ are in MM states. Wright (2004) claims that without knowing $\log(g)$ or the height above the main sequence, it is easy to confuse subgiants with MM stars. This was problematic both because subgiants have inherently lower activity, so they can fall in the same parameter space as MM stars, and because the search for stars in states of magnetic minima is more compelling for Sun-like stars. If the conclusions from Wright (2004) are correct, we expect stars with $\log(R'_{\text{HK}}) < -5.1$ to be evolved stars. The bottom row of Figure 6 shows stars with smaller radii are more active, populating the “Inactive” and “Active” bins. Our three best candidates above are distinctly not subgiants. We have an unusually large number of stars relative to the nearby star catalogs, with a full population of stars with $\log(R'_{\text{HK}}) < -5.1$.

Hall et al. (2007) studied 18 solar-type stars and concluded that $\log(R'_{\text{HK}})$ is not a good metric to identify stars in a magnetic minimum state. This is due to the unknown effects of metallicity and stellar surface gravity. They claimed that a better metric is delta F_{HK} , which is the measure of the flux caused by magnetic activity in the H and K lines. It is robust against high stellar rotation as well. This agrees with Saar (2006), who noted that the minimum activity of a star is dependent on metallicity. Specifically, metal-poor dwarfs have a higher minimum $\log(R'_{\text{HK}})$ than dwarfs of solar metallicity.

X-rays play an important role in observing and assessing chromospheric activity and searching for MM stars because it is difficult to explain the creation of X-rays without the magnetic field processes associated with chromospheric activity detected in the optical. We defer the incorporation of X-ray data for future work.

Wright (2004) had precise parallaxes from Hipparcos but lacked precise metallicity and stellar surface gravity required to separate their relationship to stellar activity. We now have excellent metallicities, so we can check if stars that are below the main sequence are very metal-poor. Saar (2011) provided a

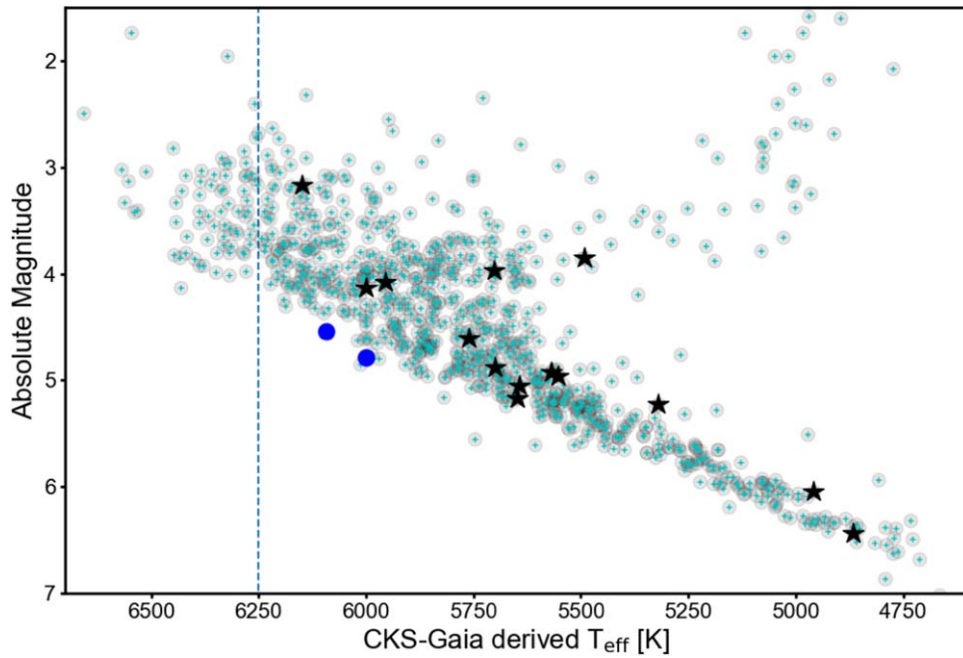


Figure 17. This color–magnitude diagram highlights several subcategories of stars and allows for identification of Maunder minimum candidate stars, following the logic of Wright (2004). We plot the CKS–HK stellar sample as the gray background of data points. Black star symbols highlight exceptionally metal-poor stars with $[\text{Fe}/\text{H}] < -0.4$. Blue circles represent stars that are 0.4 magnitudes below the main sequence and are “very inactive” with $\log(R'_{\text{HK}}) < -5.2$ as the threshold. Stars of very low stellar activity that fall below the main sequence are candidates for MM status. The vertical line denotes the temperature of the Kraft Break, above which we do not expect stars to have an active convective zone contributing to stellar activity. The two blue data points are KOI-4144 and KOI-5236. (KOI-1531 misses the $\log(R'_{\text{HK}}) < -5.2$ cutoff).

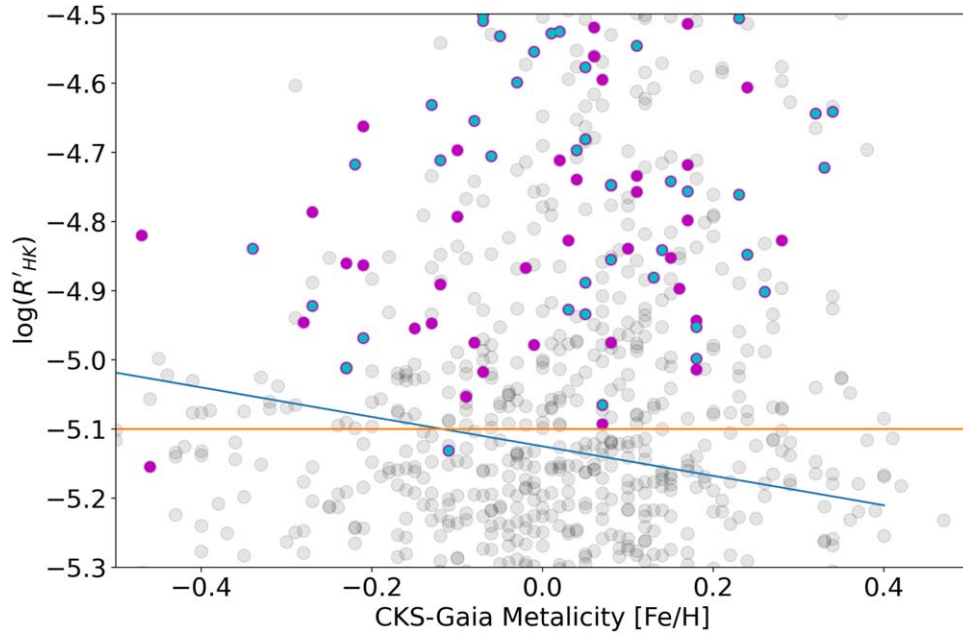


Figure 18. We search for the dependence of metallicity on the lowest level of activity for dwarf stars. Inspired by Saar (2011, their Figure 2), we examine metallicity vs. $\log(R'_{\text{HK}})$, with the blue diagonal line representing a minimum activity as a function of metallicity for dwarf stars. Our full set of 879 stars is shown in gray, with magenta stars representing stars with T_{eff} less than 5300 K and the cyan stars have delta magnitude above the main sequence of greater than 0.5. According to the criteria from Saar (2011), these are candidate MM stars, but knowing something about their long-term variability is also required. Since we do not have that with our sample, they must remain candidates. Contrary to Saar (2011), we do not see a dependence on metallicity for low-activity stars. Perhaps a sample of extremely low-metallicity stars would offer a stronger case for a correlation between activity and metallicity.

functional cutoff of in the plotting of $\log(R'_{\text{HK}})$ as a function of metallicity.

Using a similar analysis to Saar (2011), we can plot chromospheric activity as function of stellar metallicity, limit our search to dwarf stars, and identify the least active stars.

Broadly speaking, we do not see the trend of minimum $\log(R'_{\text{HK}})$ that is noted by Saar (2011). Note that we lack many stars beyond ± 0.4 dex that give the most leverage in assessing effects of metallicity. Figure 18 shows no visible trend in metallicity for stars in the CKS–HK sample, although

with limited parameter space. Specifically, we find that KOI-241 and KOI-2498 are the two least active stars, and confirm, by eye, that they have high-quality S -values. They are both quite cool stars compared to the solar temperature inactive stars that were previously discussed, with T_{eff} of 4960 and 5128 K, respectively. Their metallicities are -0.46 and -0.11 . The David et al. (2021) rotation periods are 32.7 days and 15.2, respectively, but both are listed as ambiguous or lacking a clear cycle. An additional test would be to check the stars' variation over time. With only single-epoch measurements, we can only say these stars are currently in low activity states, but not necessarily in extended MM states.

3.5.2. Activity, Close-in Planets, and Toroidal Gas Rings

The work of Fossati et al. (2013) revealed that the star system hosting ultra-short-period hot-Jupiter planet WASP-12b shows evidence of a gas ring surrounding the star, which is due to excessively low flux in the Mg II H and K lines, located at 2586 Å. The Ca II H and K lines confirm this interpretation along with measurements of the strongly varying near-UV flux. We searched for similar occurrences of incredibly low $\log(R'_{\text{HK}})$ values around similar-type planet hosting systems and find none as compelling as WASP-12, which has a $\log(R'_{\text{HK}})$ value of -5.50 and T_{eff} 6250 K.

We searched our sample for stars with a T_{eff} between 5800 and 6250 K, planet orbital periods less than 1 day, and stellar surface gravity greater than 4.2, bracketing the properties of the WASP-12 system. Of the two systems that have planet radii larger than ten Earth-radii, both are eclipsing binaries from CFOP (Gautier et al. 2010). For planets with radii < 10 Earth-radii and the same stellar property limitations as previously listed, 10 systems remain, the largest with a planet radius of 3 Earth-radii. Three stars have $\log(R'_{\text{HK}}) < -5.2$. KOI-2717 has a $\log(R'_{\text{HK}})$ value $= -5.226$ and shows visible evidence of emission below the solar level, in a high-S/N spectrum. KOI-4072 ($\log(R'_{\text{HK}}) = -5.241$) and KOI-4144 ($\log(R'_{\text{HK}}) = -5.306$) show modest evidence of a very low flux, but the S/N makes visual confirmation difficult. Reobservation of these three stars at higher S/N could help confirm their activity level. Figure 19 shows WASP-12 Ca II H and K spectral features along with the three most inactive stars in our survey. We do not find convincing evidence of a toroidal gas ring, although our survey does not contain many hot Jupiters. Transit surveys such as TESS will detect many transiting bright stars enabling a larger survey of stars to search toroidal gas rings.

Kepler stars are more metal-rich than the solar neighborhood, so the paucity of hot Jupiters is not related to metallicity in a similar way to the hot-Jupiter occurrence in the solar neighborhood (Petigura et al. 2018). The bias of the Kepler sample also contains a large number of subgiants that have inherently lower chromospheric emission. Using a sample of Sun-like stars hosting hot Jupiters would provide a more complete search space than the CKS sample of transiting planet hosts. Using a large sample of hot-Jupiter host star spectra to search for such anomalous emission is more promising than using the CKS-HK data set.

Future work on this could include examination of the Rossiter McLaughlin sequences of inflated hot Jupiters to search for variations in the S -values over the course of the transit. Similarly, if a large sample of hot Jupiters were sampled such as those found by TESS, perhaps more stars similar to WASP-12 would be found.

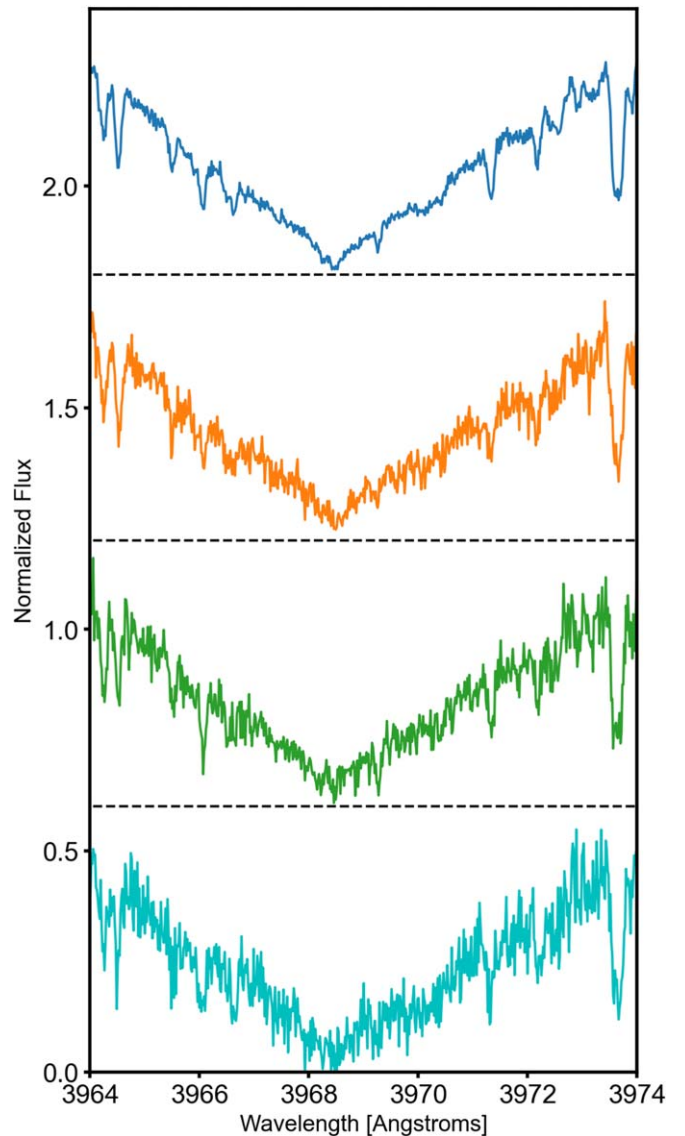


Figure 19. These four spectra represent the four most inactive stars in our survey. Each star is vertically offset with the dotted line representing zero flux. The top panel shows WASP-12 with exceptionally low activity and a spectrum with high S/N. The bottom three plots show that for stars with very little activity, it is difficult to visually distinguish between inactive and very inactive stars. Below WASP-12 are KOI-2786, KOI-2906, and KOI-2833. Their $\log(R'_{\text{HK}})$ values are -6.122 , -5.994 , and -5.962 , respectively.

3.6. Planet Radii and Chromospheric Activity

Identification of the small planet radius gap (Fulton gap) at roughly $1.8 R_{\text{Earth}}$ both theoretically and observationally has been of great interest to planet formation theory. Stellar insolation at the planets' average orbital distance is strongly correlated with planet radius on the small side of the radius gap receiving higher insolation and planets on the larger radius side receiving less. Stellar mass plays a critical role in shaping the exact radius at which the gap falls (Petigura et al. 2022) and predictions of the time frame over which the gap is sculpted range from < 1 Gyr (Berger et al. 2020a) to several gigayear timescales (David et al. 2022).

Acknowledging that stars become less active as they age, making age and activity degenerate, we examine the relationship between activity and planet radius directly with our CKS-

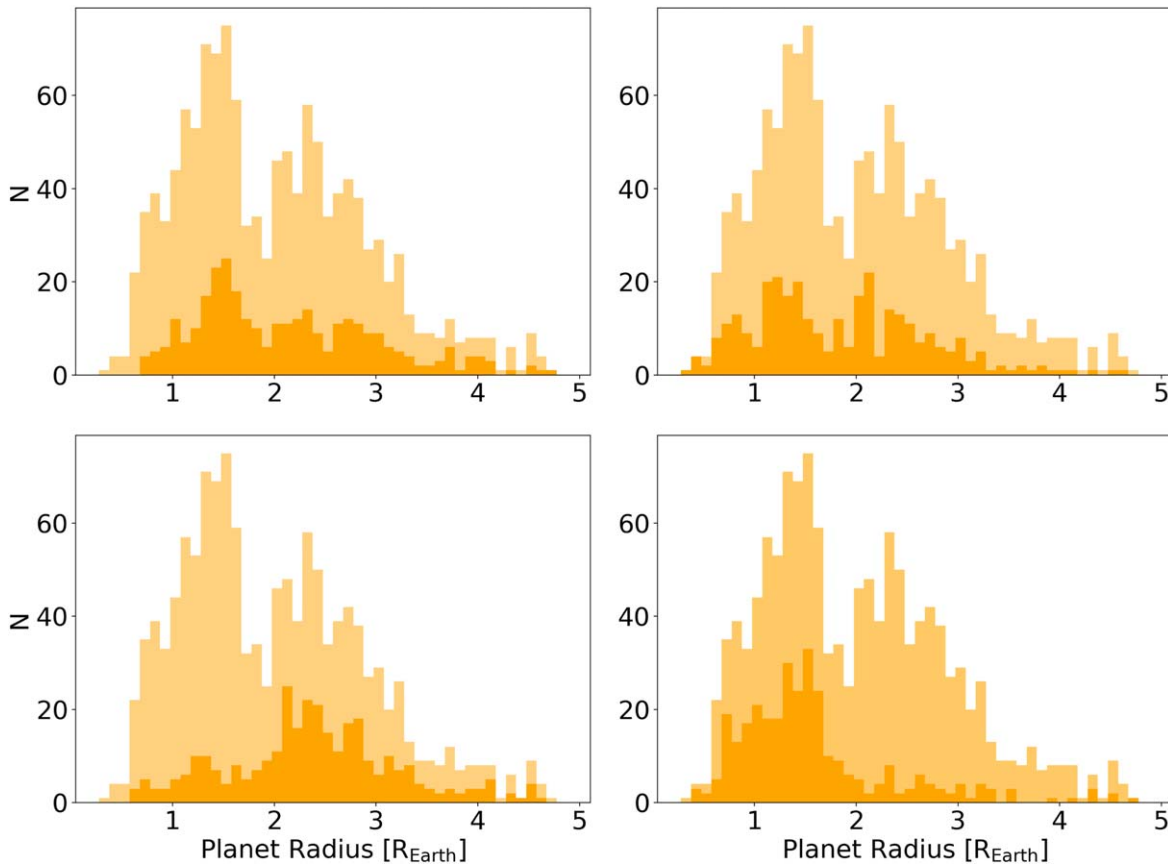


Figure 20. In the background of each plot, the CKS-HK planet population of 773 stars hosting 1243 small planets is plotted. In the two top panels, we examine the planet radius histogram to check how the super-Earth and mini-Neptune populations correspond to the most and least chromospherically active planet-host stars. Top left: with the dark color, we plot the top quartile of planets in the $\log(R'_{\text{HK}})$ distribution. Top right: with the dark color, we plot the bottom quartile of planets in the $\log(R'_{\text{HK}})$ distribution. We do not see an abundance of super-Earths in the active stars, nor an under-abundance in the sub-Neptunes as we might get if chromospheric activity was highly correlated with planet radius. The pattern present in the insolation plots is not reflected here. Bottom left: the quartile of stars with the lowest insolation is plotted in dark orange showing an overabundance of sub-Neptunes. Bottom right: the quartile of planets with the highest insolation is plotted, showing an overabundance of super-Earths. This is consistent with the results of Fulton et al. (2017).

HK planet sample. We plot histograms of the most active and least active stars and compare those planet populations to the planets with the most and least insolation flux. Figure 20 shows four histograms of the CKS-HK planet sample. Each panel shows the full sample histogram with a different subset overplotted. In the top two panels, we see the least active quartile overplotted (left) and the most active quartile (right). The bottom panels show the planets receiving the lowest quartile (left) and the highest quartile of insolation flux (right). Without absolute occurrence of planet in each bin, as was shown in Fulton & Petigura (2018), we can still identify the previously established trend of small mass planets receiving higher insolation. In the top panels, we see no obvious differences in the two quartiles that separate planet hosts in the most and least active quartiles. We expect the super-Earths to receive the most insolation and mini-Neptunes to receive less. If the present chromospheric activity of a star is correlated to the planet radius, we would expect a similar pattern in the top panels. Instead, we see a peak of super-Earths in the most chromospherically quiet stars. We also searched for trends and correlations in the $\log(R'_{\text{HK}})$ versus orbital separation parameter space and found no significant trends.

The connection between planet size and chromospheric activity is degenerate with age, complicating the interpretation. We plot the chromospheric activity versus planet radius in

Figure 21, subdividing the sample by both T_{eff} and $[\text{Fe}/\text{H}]$. For a full explanation of isochronal age dependence on the radius gap, see Berger et al. (2020a) and David et al. (2022).

4. Conclusion

We present chromospheric activity measurements of the well-studied CKS-Gaia sample of transiting planet host stars via the Ca II H and K spectral features that are known to track magnetic activity in solar-type stars. These novel measurements are used along with the fundamental stellar properties including temperature, surface gravity and metallicity, and photometric rotation periods to explore fundamental relationships in the age–rotation–activity regime of stellar astrophysics.

We have also used the chromospheric activity measurements to check for a dependency of metallicity on the rotation periods measured from photometry and the stars corresponding Rossby numbers. Using rotation periods determined from Kepler light curves, we have searched for stellar over-abundances among long and short rotation periods in the temperature–period plane. With our single-epoch spectra, we have identified very inactive stars, but we do not yet have the multiyear time series needed to verify stars in Maunder minimum (i.e., magnetic minimum)–like states.

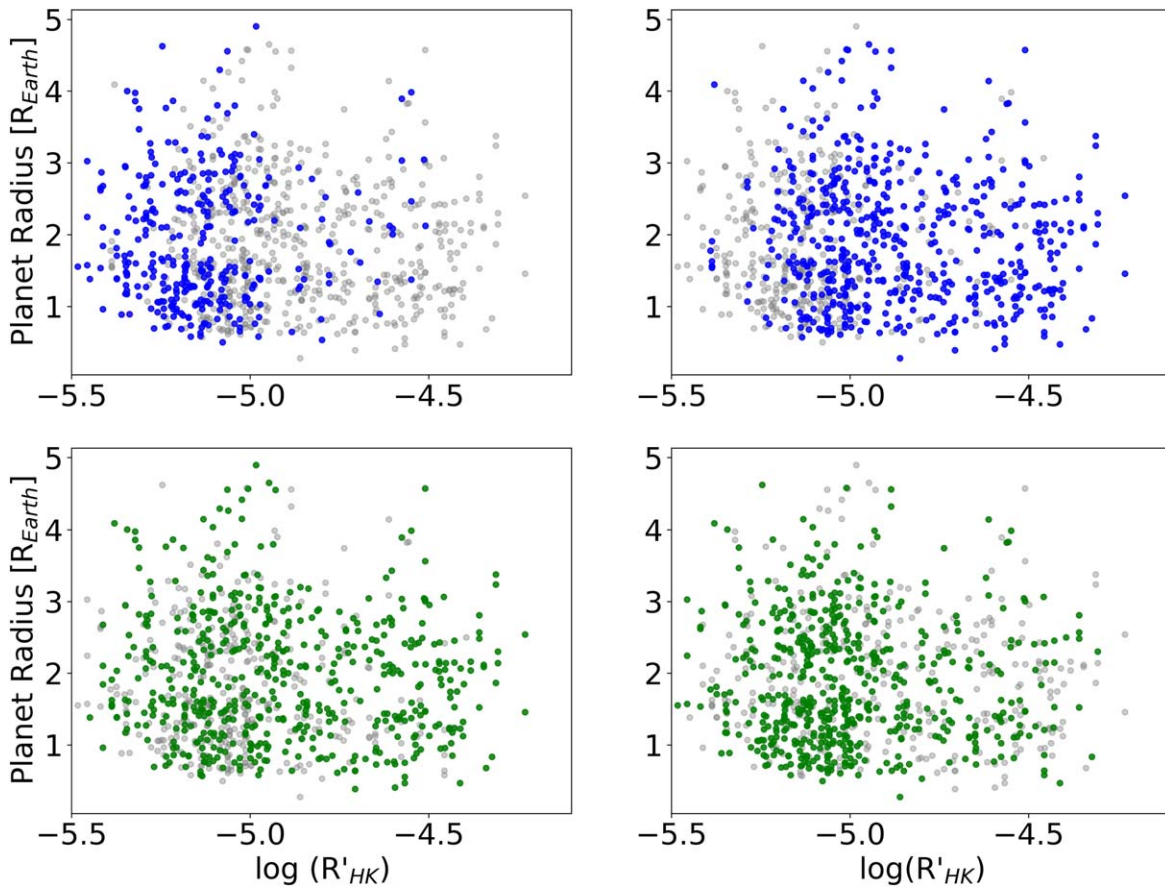


Figure 21. Planet radii as a function of chromospheric activity for Kepler’s small planets. The top panels show stars hotter than the Sun ($T_{\text{eff}} > 5770$ K, left) and those cooler than the Sun, right. The gray stars show the full sample of 912 planets that pass our quality criteria. The bottom row shows the CKS-HK sample divided at the median metallicity of 0.05 with higher metallicity on the left and lower metallicity on the right.

From the large sample of precise stellar properties and activity results presented in this paper, we find no significant evidence for metallicity-dependent activity relations within the metallicity range of -0.2 to $+0.3$. Our results are supportive of the theory of WMB of stellar spindown in the form of discrepancies between activity determined and photometrically determined rotation periods. While 1 Gyr previously has been suggested as a critical age juncture, we find no significant evidence for a change in the activity–period relationship at this age using chromospherically derived ages. The activity–period relationship presented here, along with recently discovered nuances discovered in the temperature–period plane such as the Rossby Ridge and their relative independence from stellar metallicity, can all inform future theoretical studies of stellar rotation–activity relationships, and an understanding of the physics of the underlying stellar magnetic dynamos.

Acknowledgments

The authors extend thanks to Travis Metcalfe and Luke Bouma for helpful discussions on early versions of the paper. We also thank Ryan Rubenzahl, Sarah Blunt, and Aida Behrard for providing feedback during group discussions.

Some of the data presented herein were obtained at the W. M. Keck Observatory, which is operated as a scientific partnership among the California Institute of Technology, the University of California, and the National Aeronautics and Space Administration. The Observatory was made possible by the generous financial support of the W. M. Keck Foundation. This research has made

use of NASA’s Astrophysics Data System. L.M.W. acknowledges support from the NASA-Keck Key Strategic Mission Support program (grant No. 80NSSC19K1475) and the NASA Exoplanet Research Program (grant No. 80NSSC23K0269). Support was provided by the Simons Foundation grant “Planetary Context of Habitability and Exobiology”.

The authors wish to recognize and acknowledge the very significant cultural role and reverence that the summit of Maunakea has always had within the indigenous Hawaiian community. We are most fortunate to have the opportunity to conduct observations from this mountain.

This project would not have been possible without major allocations of Keck telescope time from the University of California, California Institute of Technology, the University of Hawaii, and NASA. This work utilized the Exoplanet Archive, SIMBAD, the Community Follow-up Program, and data from NASA’s Kepler Space Telescope.

Facility: Keck:I (HIRES), Kepler

Software: We made use of the following publicly available Python modules: astropy (Astropy Collaboration et al. 2013), matplotlib (Hunter 2007), numpy/scipy (van der Walt et al. 2011), and pandas (McKinney 2010). Interactive Data Language (IDL) was used to extract the spectral line information.

ORCID iDs

Howard Isaacson <https://orcid.org/0000-0002-0531-1073>
 Stephen R. Kane <https://orcid.org/0000-0002-7084-0529>
 Brad Carter <https://orcid.org/0000-0002-7084-0529>

Andrew W. Howard  <https://orcid.org/0000-0001-8638-0320>

Lauren Weiss  <https://orcid.org/0000-0002-3725-3058>

Erik A. Petigura  <https://orcid.org/0000-0003-0967-2893>

Benjamin Fulton  <https://orcid.org/0000-0003-3504-5316>

References

- Aigrain, S., Pont, F., & Zucker, S. 2012, *MNRAS*, **419**, 3147
- Akana Murphy, J. M., Kosiarek, M. R., Batalha, N. M., et al. 2021, *AJ*, **162**, 294
- Amard, L., & Matt, S. P. 2020, *ApJ*, **889**, 108
- Angus, R., Morton, T., Aigrain, S., Foreman-Mackey, D., & Rajpaul, V. 2018, *MNRAS*, **474**, 2094
- Astropy Collaboration, Robitaille, Thomas P., Tollerud, Erik J., et al. 2013, *A&A*, **558**, A33
- Avallone, E. A., Tayar, J. N., van Saders, J. L., et al. 2022, *ApJ*, **930**, 7
- Baliunas, S. L., Donahue, R. A., Soon, W. H., et al. 1995, *ApJ*, **438**, 269
- Batalha, N. M., Borucki, W. J., Bryson, S. T., et al. 2011, *ApJ*, **729**, 27
- Batalha, N. M., Rowe, J. F., Bryson, S. T., et al. 2013, *ApJS*, **204**, 24
- Baum, A. C., Wright, J. T., Luhn, J. K., & Isaacson, H. 2022, *AJ*, **163**, 183
- Berger, T. A., Huber, D., Gaidos, E., van Saders, J. L., & Weiss, L. M. 2020a, *AJ*, **160**, 108
- Berger, T. A., Huber, D., van Saders, J. L., et al. 2020b, *AJ*, **159**, 280
- Blunt, S., Carvalho, A., David, T. J., et al. 2023, *AJ*, **166**, 62
- Borucki, W. J., Agol, E., Fressin, F., et al. 2013, *Sci*, **340**, 587
- Borucki, W. J., Koch, D. G., Basri, G., et al. 2011a, *ApJ*, **728**, 117
- Borucki, W. J., Koch, D. G., Basri, G., et al. 2011b, *ApJ*, **736**, 19
- Borucki, W. J., Koch, D. G., Brown, T. M., et al. 2010, *ApJL*, **713**, L126
- Brandenburg, A., Mathur, S., & Metcalfe, T. S. 2017, *ApJ*, **845**, 79
- Chen, H., & Rogers, L. A. 2016, *ApJ*, **831**, 180
- Christiansen, J. L., Jenkins, J. M., Caldwell, D. A., et al. 2012, *PASP*, **124**, 1279
- Curtis, J. L., Agüeros, M. A., Matt, S. P., et al. 2020, *ApJ*, **904**, 140
- Dai, F., Winn, J. N., Schlaufman, K., et al. 2020, *AJ*, **159**, 247
- David, T. J., Angus, R., Curtis, J. L., et al. 2022, *ApJ*, **933**, 114
- David, T. J., Contardo, G., Sandoval, A., et al. 2021, *AJ*, **161**, 265
- Duncan, D. K., Vaughan, A. H., Wilson, O. C., et al. 1991, *ApJS*, **76**, 383
- Eddy, J. A. 1976, *Sci*, **192**, 1189
- Fossati, L., Ayres, T. R., Haswell, C. A., et al. 2013, *ApJL*, **766**, L20
- Fulton, B. J., & Petigura, E. A. 2018, *AJ*, **156**, 264
- Fulton, B. J., Petigura, E. A., Howard, A. W., et al. 2017, *AJ*, **154**, 109
- Fulton, B. J., Weiss, L. M., Sinukoff, E., et al. 2015, *ApJ*, **805**, 175
- Gautier, T. N., Batalha, N. M., Borucki, W. J., et al. 2010, arXiv:1001.0352
- Gomes da Silva, J., Santos, N. C., Adibekyan, V., et al. 2021, *A&A*, **646**, A77
- Hall, J. C., Lockwood, G. W., & Skiff, B. A. 2007, *AJ*, **133**, 862
- Hall, O. J., Davies, G. R., van Saders, J., et al. 2021, *NatAs*, **5**, 707
- Henry, T. J., Soderblom, D. R., Donahue, R. A., & Baliunas, S. L. 1996, *AJ*, **111**, 439
- Howard, A. W., Sanchis-Ojeda, R., Marcy, G. W., et al. 2013, *Natur*, **503**, 381
- Hsu, D. C., Ford, E. B., Ragozzine, D., & Ashby, K. 2019, *AJ*, **158**, 109
- Hunter, J. D. 2007, *CSE*, **9**, 90
- Isaacson, H., & Fischer, D. 2010, *ApJ*, **725**, 875
- Johnson, J. A., Petigura, E. A., Fulton, B. J., et al. 2017, *AJ*, **154**, 108
- Judge, P. G., & Saar, S. H. 2007, *ApJ*, **663**, 643
- Kolbl, R., Marcy, G. W., Isaacson, H., & Howard, A. W. 2015, *AJ*, **149**, 18
- Kosiarek, M. R., & Crossfield, I. J. M. 2020, *AJ*, **159**, 271
- Kraft, R. P. 1967, *ApJ*, **150**, 551
- Lissauer, J. J., Marcy, G. W., Bryson, S. T., et al. 2014, *ApJ*, **784**, 44
- Lopez, E. D., & Fortney, J. J. 2013, *ApJ*, **776**, 2
- Lubin, J., Robertson, P., Stefansson, G., et al. 2021, *AJ*, **162**, 61
- Luhn, J. K., Wright, J. T., Henry, G. W., Saar, S. H., & Baum, A. C. 2022, *ApJL*, **936**, L23
- Mamajek, E. E., & Hillenbrand, L. A. 2008, *ApJ*, **687**, 1264
- Masuda, K. 2022, *ApJ*, **933**, 195
- Mayor, M., & Queloz, D. 1995, *Natur*, **378**, 355
- Mazeh, T., Perets, H. B., McQuillan, A., & Goldstein, E. S. 2015, *ApJ*, **801**, 3
- McKinney, W. 2010, in Proc. of the 9th Python in Science Conf., ed. S. van der Walt & J. Millman, 56
- McQuillan, A., Mazeh, T., & Aigrain, S. 2014, *ApJS*, **211**, 24
- Metcalfe, T. S., & Egeland, R. 2019, *ApJ*, **871**, 39
- Metcalfe, T. S., Egeland, R., & van Saders, J. 2016, *ApJL*, **826**, L2
- Mittag, M., Schmitt, J. H. M. M., & Schröder, K. P. 2013, *A&A*, **549**, A117
- Noyes, R. W., Hartmann, L. W., Baliunas, S. L., Duncan, D. K., & Vaughan, A. H. 1984, *ApJ*, **279**, 763
- Owen, J. E., & Wu, Y. 2013, *ApJ*, **775**, 105
- Pepe, F., Cameron, A. C., Latham, D. W., et al. 2013, *Natur*, **503**, 377
- Perryman, M. A. C., Lindgren, L., Kovalevsky, J., et al. 1997, *A&A*, **323**, L49
- Petigura, E. A. 2020, *AJ*, **160**, 89
- Petigura, E. A., Howard, A. W., Marcy, G. W., et al. 2017, *AJ*, **154**, 107
- Petigura, E. A., Marcy, G. W., Winn, J. N., et al. 2018, *AJ*, **155**, 89
- Petigura, E. A., Rogers, J. G., Isaacson, H., et al. 2022, *AJ*, **163**, 179
- Rosenthal, L. J., Fulton, B. J., Hirsch, L. A., et al. 2021, *ApJS*, **255**, 8
- Rowe, J. F., Bryson, S. T., Marcy, G. W., et al. 2014, *ApJ*, **784**, 45
- Saar, S. H. 2006, AAS/SPD Meeting, **37**, 12.01
- Saar, S. H. 2011, in ASP Conf. Ser. 448, 16th Cambridge Workshop on Cool Stars, Stellar Systems, and the Sun, ed. C. Johns-Krull, M. K. Browning, & A. A. West (San Francisco, CA: ASP), 1239
- Sanchis-Ojeda, R., Rappaport, S., Winn, J. N., et al. 2014, *ApJ*, **787**, 47
- Santos, A. R. G., Breton, S. N., Mathur, S., & García, R. A. 2021, *ApJS*, **255**, 17
- Shah, S. P., Wright, J. T., Isaacson, H., Howard, A. W., & Curtis, J. L. 2018, *ApJL*, **863**, L26
- Skumanich, A. 1972, *ApJ*, **171**, 565
- Su, T., Zhang, L.-y., Long, L., et al. 2022, *ApJS*, **261**, 26
- Thompson, S. E., Coughlin, J. L., Hoffman, K., et al. 2018, *ApJS*, **235**, 38
- Valenti, J. A., & Fischer, D. A. 2005, *ApJS*, **159**, 141
- van der Walt, S., Colbert, S. C., & Varoquaux, G. 2011, *CSE*, **13**, 22
- Van Eylen, V., Agentoft, C., Lundkvist, M. S., et al. 2018, *MNRAS*, **479**, 4786
- van Saders, J. L., Ceillier, T., Metcalfe, T. S., et al. 2016, *Natur*, **529**, 181
- Vaughan, A. H., Preston, G. W., & Wilson, O. C. 1978, *PASP*, **90**, 267
- Walkowicz, L. M., & Basri, G. S. 2013, *MNRAS*, **436**, 1883
- Weiss, L. M., Marcy, G. W., Petigura, E. A., et al. 2018, *AJ*, **155**, 48
- Wright, J. T. 2004, *AJ*, **128**, 1273
- Wright, J. T., Marcy, G. W., Butler, R. P., et al. 2008, *ApJL*, **683**, L63
- Wright, J. T., Marcy, G. W., Butler, R. P., & Vogt, S. S. 2004, *ApJS*, **152**, 261
- Zhang, J., Bi, S., Li, Y., et al. 2020, *ApJS*, **247**, 9